CM^2 Magazine

第 134 期

南方科技大学海洋磁学中心主编

https://cm2.sustech.edu.cn/

创刊词

海洋是生命的摇篮，是文明的纽带。地球上最早的生命诞生于海洋，海洋里的生命最终进化成了人类，人类的文化融合又通过海洋得以实现。人因海而兴。

人类对海洋的探索从未停止。从远古时代美丽的神话传说，到麦哲伦的全球航行，再到现代对大洋的科学钻探计划，海洋逐渐从人类敬畏崇拜幻想的精神寄托演变成可以开发利用与科学研究的客观存在。其中，上个世纪与太空探索同步发展的大洋科学钻探计划将人类对海洋的认知推向了崭新的纬度：深海（deep sea）与深时（deep time）。大洋钻探计划让人类知道，奔流不息的大海之下，埋藏的却是亿万年的地球历史。它们记录了地球板块的运动，从而使板块构造学说得到证实；它们记录了地球环境的演变，从而让古海洋学方兴未艾。

在探索海洋的悠久历史中，从大航海时代的导航，到大洋钻探计划中不可或缺的磁性地层学，磁学发挥了不可替代的作用。这不是偶然，因为从微观到宏观，磁性是最基本的物理属性之一，可以说，万物皆有磁性。基于课题组的学科背景和对海洋的理解，我们对海洋的探索以磁学为主要手段，海洋磁学中心因此而生。

海洋磁学中心，简称 CM^2，一为其全名“Centre for Marine Magnetism”的缩写，另者恰与爱因斯坦著名的质能方程 $E = MC^2$ 对称，借以表达我们对科学巨匠的敬仰和对科学的不懈追求。

然而科学从来不是单打独斗的产物。我们以磁学为研究海洋的主攻利器，但绝不仅限于磁学。凡与磁学相关的领域均是我们关注的重点。为了跟踪反映国内外地球科学特别是与磁学有关的地球科学领域的最新研究进展，海洋磁学中心特地主办 CM^2 Magazine，以期与各位地球科学工作者相互交流学习、合作共进！

“海洋孕育了生命，联通了世界，促进了发展”。21 世纪是海洋科学的时代，由陆向海，让我们携手迈进中国海洋科学的黄金时代。

目 录

1. 亚热带云是南大洋连接热带太平洋的关键所在

翻译人：仲义 zhongy@sustech.edu.cn

Kim H.J., Kang, S.M., Kay, J.E., et al. ***Subtropical clouds key to Southern Ocean teleconnections to the tropical Pacific*** *[J] Proceedings of the National Academy of Sciences, 2022, 119(34), e2200514119.*

https://doi.org/10.1073/pnas.2200514119

摘要：热带太平洋东南部地区的大量降水是一个贯穿于数代全球气候模式的普遍现象。虽然最新研究表明过度温暖的南大洋是其主要原因，但是根据海洋环流反馈过程，模型在这种远程传输的机制定量上存在分歧。本文中，作者利用南大洋地区辐射冷却的多模式实验，显示了由亚热带短波云反馈介导的南大洋到热带太平洋的遥相关作用。南大洋降温优先冷却东南热带太平洋，从而使得热带太平洋东部雨带北移，降水减少。区域性云锁定实验证实，遥相关效率依赖于亚热带层积云反馈。在大多数气候模型中，这种亚热带云的反馈太弱了，表明从南大洋到热带太平洋的遥相关作用比人们普遍认为的要强。

ABSTRACT: Excessive precipitation over the southeastern tropical Pacific is a major common bias that persists through generations of global climate models. While recent studies suggest an overly warm Southern Ocean as the cause, models disagree on the quantitative importance of this remote mechanism in light of ocean circulation feedback. Here, using a multimodel experiment in which the Southern Ocean is radiatively cooled, we show a teleconnection from the Southern Ocean to the tropical Pacifi c that is mediated by a shortwave subtropical cloud feedback. Cooling the Southern Ocean preferentially cools the southeastern tropical Pacifi c, thereby shifting the eastern tropical Pacifi c rainbelt northward with the reduced precipitation bias. Regional cloud locking experiments confirm that the teleconnection efficiency depends on subtropical stratocumulus cloud feedback. This subtropical cloud feedback is too weak in most climate models, suggesting that teleconnections from the Southern Ocean to the tropical Pacific are stronger than widely thought.

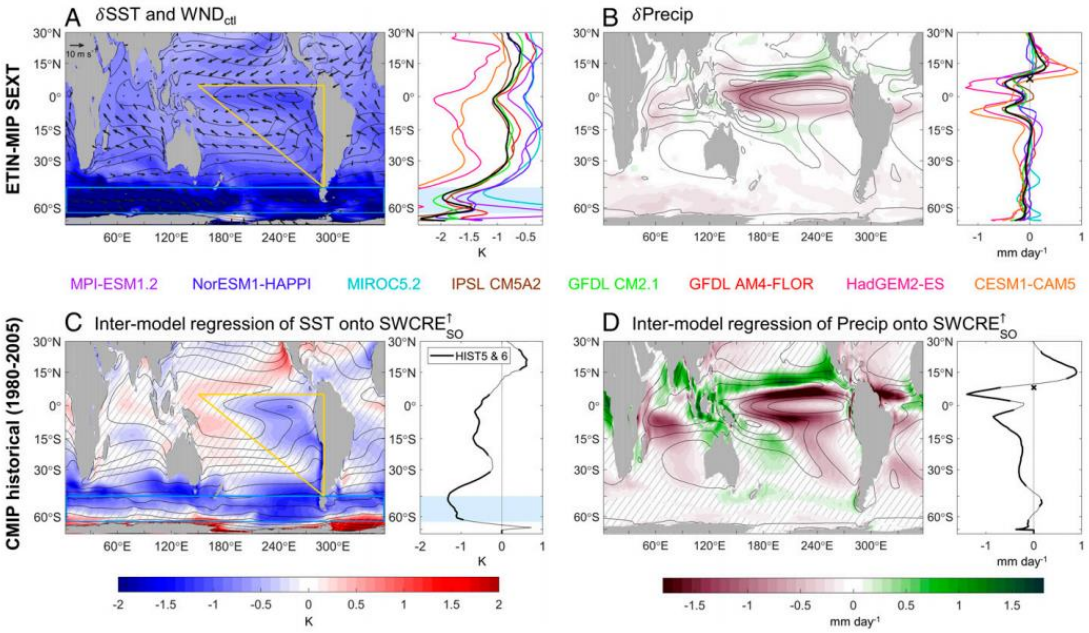

Figure 1. The impact of Southern Ocean cooling on the tropical Pacific. The multimodel mean responses averaged over years 101 –150 in (A) SST and (B) precipitation for the ETIN-MIP SEXT simulations. In A, the multimodel mean climatological surface winds are shown in arrows. The respective right panel shows the eastern Pacific average in each model, with the multimodel mean in black. Intermodel regression of the annual-mean (C) SST and (D) precipitation onto the upward SWCRE over 65°S–45°S (SWCRE "SO) using historical simulations of 39 CMIP5 and 52 CMIP6 models averaged between 1980 and 2005 (SI Appendix, Table S1 for model list). The regression coefficients are multiplied by two intermodel SDs of SWCRESO, comparable to the forcing amplitude of ETIN-MIP SEXT (SI Appendix, Fig. S1), to ease comparison with the ETIN-MIP results. The respective right panel shows the eastern Pacific (230°E–300°E) average. The region with the regression coefficients statistically different from zero is unhatched in the maps and denoted as thicker lines for the eastern Pacific average, determined via two-sided Student t test with 95% confidence interval. In A and C, the forcing region between 65°S and 45°S is indicated by blue rectangles, and the triangular cooling patch is marked by yellow triangles. In B and D, the multimodel mean position of the climatological eastern Pacific ITCZ, defined by the precipitation maximum, is denoted with a cross symbol. The contours in maps indicate the corresponding multimodel mean climatology.

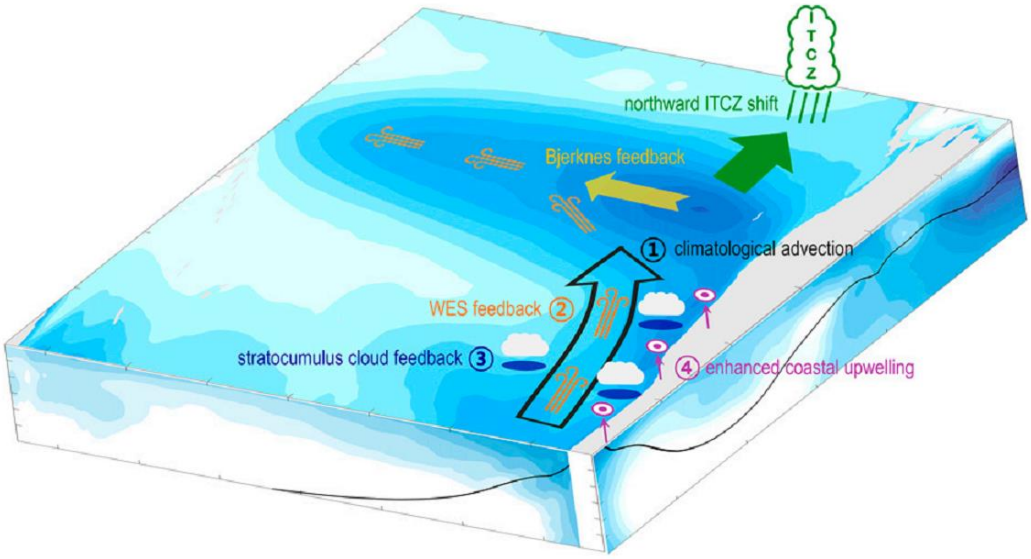

Figure 2. Schematic of Southern Ocean–tropics teleconnection mechanism. The Southern Ocean cooling propagated into the subtropics by the atmospheric eddies and oceanic Ekman transport is (1) further advected equatorward by the climatological southeasterlies (black arrow) west of South America. The southeastern Pacific cooling is amplified by the interactions between (2) WES feedback, (3) subtropical stratocumulus cloud feedback, and (4) coastal upwelling. The eastern equatorial Pacific cooling is further intensified via Bjerknes feedback. As a consequence, the triangular cooling patch extending from the southeastern Pacific to the zonal band across the equatorial Pacific is manifested by the Southern Ocean–driven teleconnection, inducing the northward shift of the eastern Pacific ITCZ.

2. Li 同位素重建脊椎动物生态学

翻译人：蒋晓东 jiangxd@sustech.edu.cn

Thibon F, Goedert J, Séon N et al. ***The ecology of modern and fossil vertebrates revisited by lithium isotopes*** *[J]. Earth and Planetary Science Letters, (2022), 599, 117840.*
https://doi.org/10.1016/j.epsl.2022.117840

摘要：脊椎动物化石记录了大量水生和陆地环境之间的转变，但其原因仍有争议。因此，对生活环境的盐度进行量化，对于精确确定生态转变的顺序至关重要。在这里，我们测量了来自不同水环境的现存和灭绝脊椎动物矿化组织的锂稳定同位素组成（δ^7Li_{mt}）：海水、淡水/陆地和“过渡环境”(即半咸水，或季节性淡水和海水)。我们报告海水脊椎动物的 δ^7Li_{mt} 值在统计上高于淡水脊椎动物，这是单独考虑的分类组。此外，生活在过渡环境中的脊椎动物具有中等的 δ^7Li_{mt} 值。因此，我们的研究表明，无论是现存的脊椎动物还是灭绝的脊椎动物，δ^7Li_{mt} 值都可以区分它们的水生栖息地。

ABSTRACT: The vertebrate fossil record documents a plethora of transitions between aquatic and terrestrial environments but their causes are still debated. Quantifying the salinity of living environments is therefore crucial for precising the sequence of ecological transitions. Here, we measured lithium stable isotope composition of mineralized tissues (δ^7Li_{mt}) of extant and extinct vertebrates from various aquatic environments: seawater, freshwater/terrestrial, and “transitional environments” (i.e. brackish waters, or seasonal access to freshwater and seawater). We report statistically higher δ^7Li_{mt} values for seawater vertebrates than freshwater ones, taxonomic groups considered separately. Moreover, vertebrates living in transitional environments have intermediate δ^7Li_{mt} values. Therefore, we show that δ^7Li_{mt} values of both extant and extinct vertebrates can discriminate their aquatic habitat.

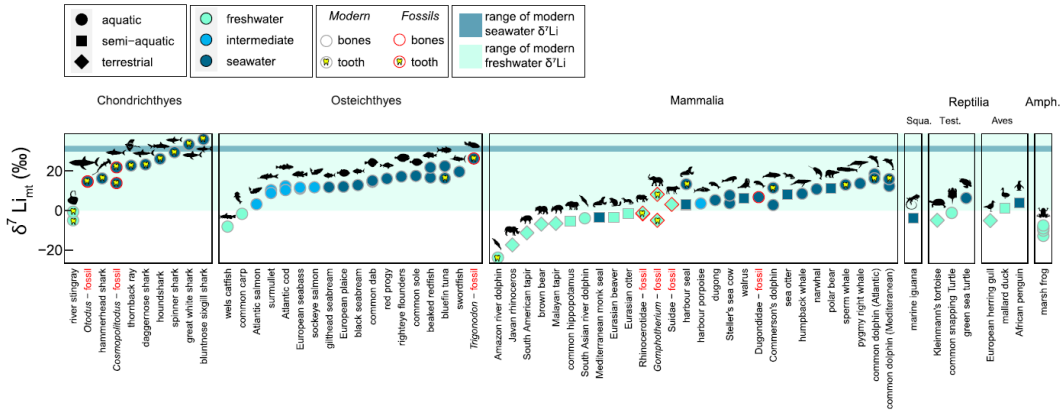

Figure 1. δ^7Li_{mt} values of modern and fossil vertebrates including Chondrichthyes, Osteichthyes, Mammalia, Reptilia, and Amphibia.Each icon represents an independent individual, except when tooth and bone from the same individual were sampled. Squa. for Squamata, Test. for Testudinea, Amph. for Amphibia. Vertebrates living in seawater have, on average, higher δ^7Li_{mt} values than those living in intermediate environments, which in turn display higher δ^7Li_{mt} values than vertebrates depending on freshwater. SD are included in the size of the markers.

3. 260 千年以来东亚夏季风的岁差驱动

翻译人：盖聪聪 gaicc@sustech.edu.cn

Guo B, Nie J, Stevens T, et al. ***Dominant precessional forcing of the East Asian summer monsoon since 260 ka*** *[J]. Geology, 2022. https://doi.org/10.1130/G50206.1*
https://doi.org/10.1130/G50206.1

摘要：轨道旋回对第四纪中晚期东亚夏季风（EASM）降水变化的影响是古气候研究中最复杂的问题之一。中国黄土记录表明，EASM 降水主要受控于北半球冰盖强迫的 100 千年周期。然而，石笋记录认为 EASM 降水主要表现为北半球夏季辐射强迫的 23 千年周期。为了解决这一争论，我们研究了黄土高原西部西津钻孔 260 千年（释光定年的大概上限）的高分辨率古气候记录。磁化率在间冰期具有明显的 23 千年周期，在冰期则呈现低值。磁化率的变化是成壤作用缺失造成的，以至于该参数并没有记录到 EASM 降水变化。因此，我们将反演的沙含量作为冰期 EASM 降水的替代指标，并将其与西津钻孔间冰期的对数磁化率进行拼接。这一新记录表明冰期和间冰期都由 23 千年周期主导，与石笋$\delta^{18}O$ 记录一致，都表明辐射强迫的主导作用。本研究促进了对黄土和石笋记录中 EASM 变率和强迫机制一致性理解，解决了过去季风研究中最大的争论之一。同时，这一发现也挑战了黄土高原中部记录中关于高纬冰盖强迫 EASM 的假说。

ABSTRACT: One of the most perplexing problems in paleoclimate research is how orbital cyclicities force East Asian summer monsoon (EASM) precipitation variation over the middle to late Quaternary. Chinese loess records suggest that EASM precipitation was dominated by 100 k.y. cycles controlled by Northern Hemisphere ice sheet forcing. In contrast, speleothem records suggest that EASM precipitation was dominated by 23 k.y. cycles caused by Northern Hemisphere summer insolation forcing. In order to resolve this inconsistency, we present high-resolution paleoclimate records from Xijin drill cores on the western Chinese Loess Plateau for the past 260 k.y., the rough upper limit of luminescence dating. Magnetic susceptibility (χ) shows clear 23 k.y. precessional cycles over interglacials but has constant low values over glacials. This is interpreted as indicating a lack of pedogenesis, such that χ cannot record EASM precipitation variations, rather than an

absence of EASM variation itself. To circumvent this issue, we use inversed sand content as an alternative proxy for EASM precipitation over glacials and splice this with the interglacial logarithmic χ from Xijin drill cores. This new record reveals dominant 23 k.y. cycles over both interglacials and glacials, consistent with speleothem $\delta^{18}O$ data and dominant insolation forcing. These findings allow a consistent understanding of EASM variability and forcing mechanisms from both loess and speleothem archives, resolving one of the largest debates in past monsoon research. These results challenge suggestions of high-latitude ice sheet forcing of the EASM based on slowly accumulated loess records from the central Loess Plateau.

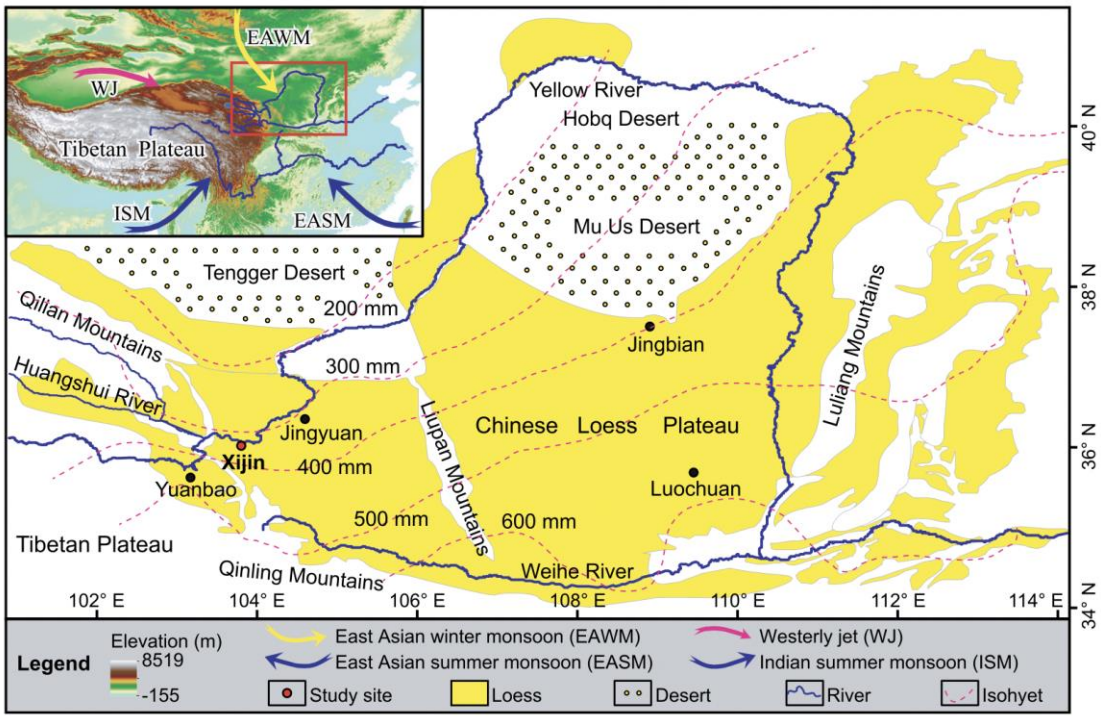

Figure 1. Map showing the geographic setting of the Chinese Loess Plateau (CLP) and surrounding mountains, deserts, and rivers. Location of the Xijin loess core in Lanzhou Basin (red circle) is shown together with locations of representative loess sections on the CLP mentioned in the text (black circles). Magenta dashed lines represent modern mean annual precipitation isohyets. Inset map shows location of the CLP in relation to the Tibetan Plateau and modern Asian atmospheric circulation systems.

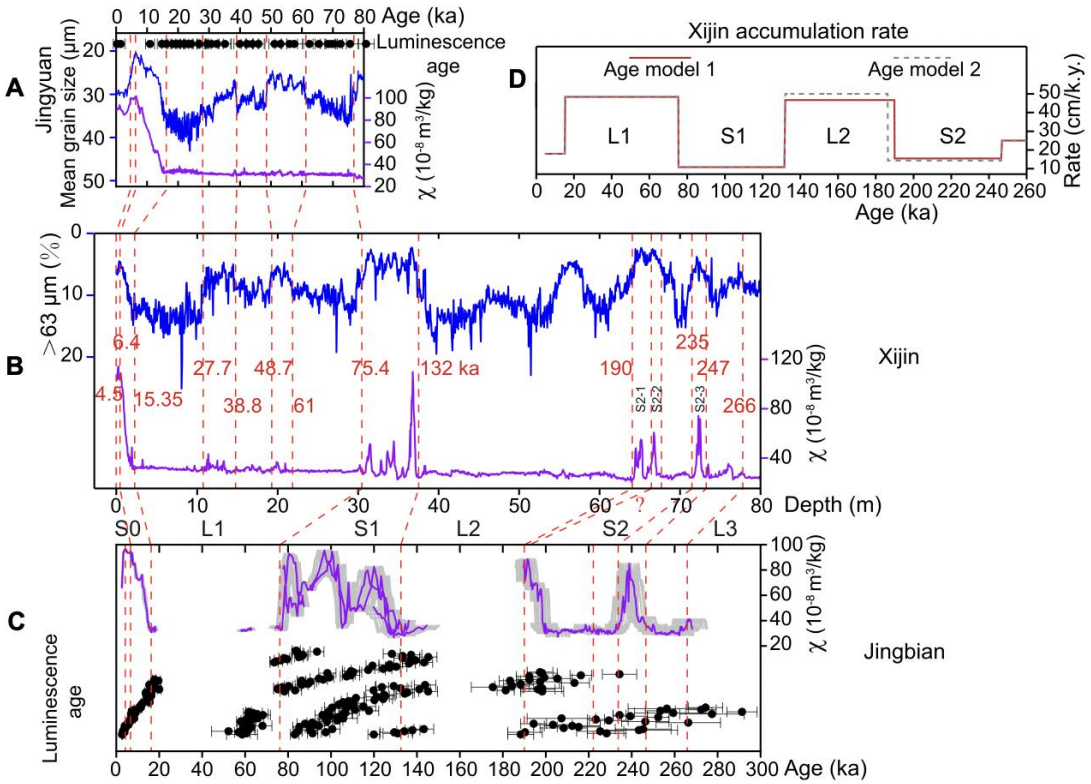

Figure 2. Establishing an age model for magnetic susceptibility (χ) and content records of Xijin cores by correlating them to independently dated χ (purple lines) and grain-size records (blue lines) on the Chinese Loess Plateau. (A) Mean-grain-size and χ records from the Jingyuan section based on high-resolution luminescence dating (black dots with vertical bars show ages and uncertainties [1σ]. (B) Sand content and χ results of Xijin cores. (C) χ records based on high-resolution luminescence dating (black dots with vertical bars show ages and uncertainties) of five loess profiles at Jingbian; gray shading associated with the χ curve indicates age model uncertainties. We note that paleosol S2 in Xijin is associated with three χ peaks (S2-1, S2-2, and S2-3), but only two are shown at Jingbian.Therefore, we established two age models for Xijin by assuming that either S2-1 or S2-2 was not recorded in Jingbian due to erosion associated with sand movement. Aligning patterns are indicated by dashed red lines, with the tie age points (ka) shown as numeric labels. (D) Loess accumulation rate records in Xijin based on two age models. L1, S1, L2, and S2 represent, from the top, loess layer 1, paleosol 1, loess layer 2, and paleosol 2, respectively.

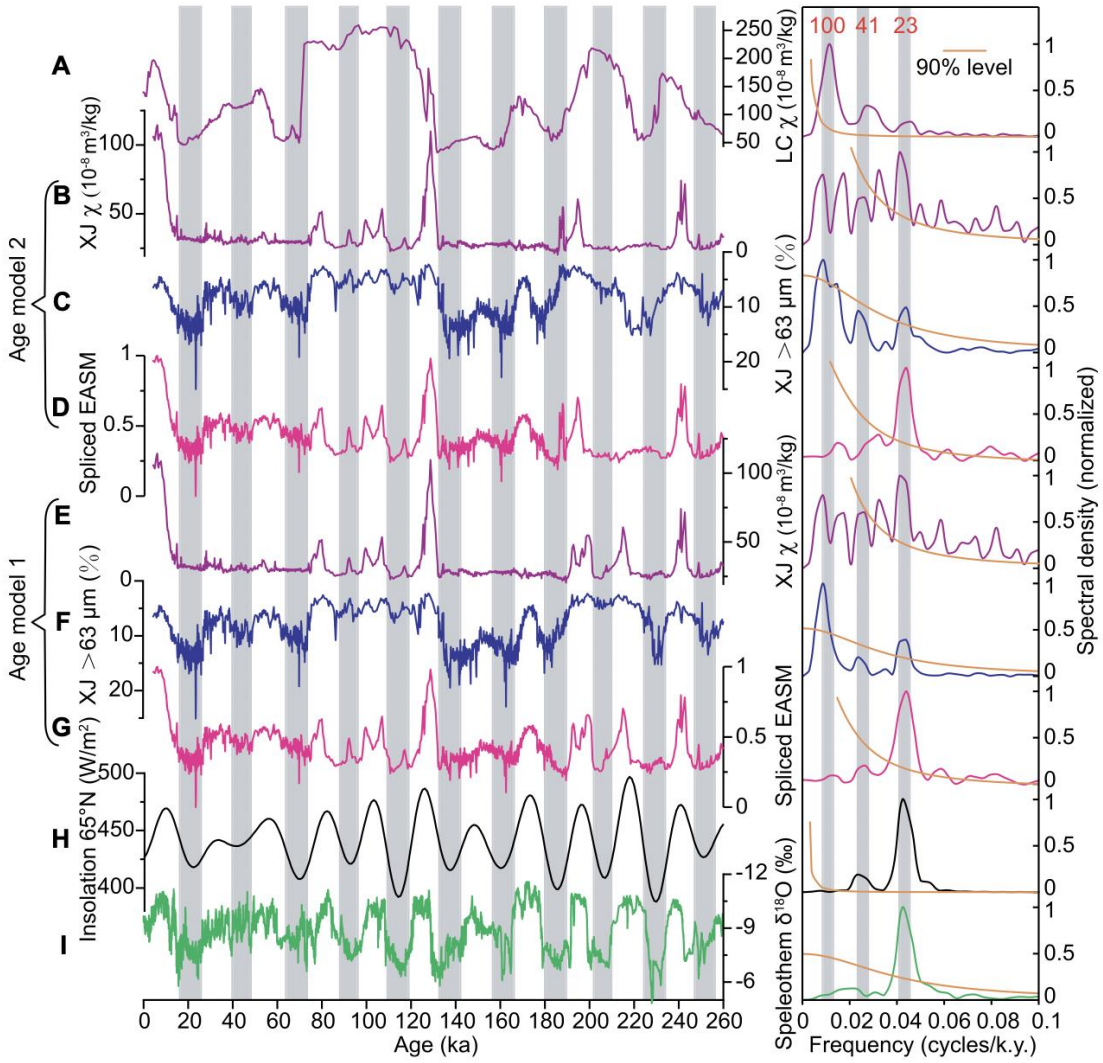

Figure 3. Time series (left) and power spectral results (right) of East Asian summer monsoon (EASM) records, based on different proxies, and summer insolation since 260 ka. (A) Magnetic susceptibility (χ) record in the Luochuan (LC) section from the central Chinese Loess Plateau (CLP). (B,C,E,F) χ (purple lines) and sand content (>63 μm [%]; blue lines) records in the Xijin (XJ) loess core under two age models. (D,G) Spliced EASM record based on the two age models (pink lines). (H) Northern Hemisphere summer insolation at 65°N (black lines). (I) Chinese speleothem δ18O records (green lines). Gray bars in the time-series data and power spectra highlight intervals of low summer insolation over the past 260 k.y. and main orbital cyclicities (100, 41, and 23 k.y.), respectively.

4. 火星富含粘土单元的水合作用：来自轨道数据与漫游者数据的对比

翻译人：张琪 zhangq7@sustech.edu.cn

Czarnecki S, Hardgrove C, Arvidson R, et al, ***Hydration of a clay-rich unit on Mars, comparison of orbital data to rover data*** *[J]. Journal of Geophysical Research: Planets, 2022.*
https://doi.org/10.1029/2021JE007104

摘要：Glen Torridon (GT)是火星盖尔环形山 Aeolis Mons 山脉的地貌特征（非正式称呼为夏普山），被当地的风化层和玄武岩沙覆盖。火星上的侦测轨道器压缩成像光谱仪(CRISM)在 GT 中检测到了粘土矿物，因此 GT 成为火星科学实验室(MSL)漫游者“好奇号”的调查目标，调查结果确认有大量的粘土存在。MSL 动态中子反照率(DAN)仪器观察到与夏普山下部地层剖面相比，漫游车横断面上的地下(< 50 cm)水化作用十分富集。在考虑到两种仪器不同的空间尺度和有效深度的情况下，本文研究了 CRISM 3 μm 水合指数与 DAN 结果的关系。作者发现，在 GT 的其中一个区域通过 CRISM 观察到的水合作用升高对应于 DAN 衍生水合作用的升高，而在另一个区域，CRISM 水合作用降低并不对应于 DAN 衍生水合作用的显著降低。作者发现，在粗糙的表面纹理和沙层覆盖区域，CRISM 测量的水合作用较低，而 DAN 的整体水合作用对这些特征相对不敏感。DAN 活性中子结果还表明，GT 地层高位具有明显的高中子吸收，这可能与富铁、富锰的成岩作用有关。此外，DAN 的结果表明，相对于其他在整个横剖面中观察到的含氢较少的单元，GT 中富含氢，这表明地下粘土矿物可能是 DAN 在 GT 中测定的水合作用的重要储层。

ABSTRACT: Glen Torridon (GT) is a geomorphic feature of Aeolis Mons (informally Mt. Sharp) in Gale crater, Mars, variably covered by local regolith and wind-blown basaltic sands. The Mars Reconnaissance Orbiter’s Compact Imaging Spectrometer for Mars (CRISM) detected clay minerals in GT, making GT a target of investigation by the Mars Science Laboratory (MSL) rover, Curiosity, which confirmed a large abundance of clays. The MSL Dynamic Albedo of Neutrons (DAN) instrument observed enrichments in bulk subsurface (< 50 cm) hydration along the rover traverse compared to lower stratigraphic sections of Mt. Sharp. Here, we investigate the relationship between the CRISM 3 μm hydration index and DAN results, taking into consideration the different

spatial scales and effective depths of these two instruments. We show that the elevated hydration observed by CRISM in one area of GT corresponds to elevated DAN-derived hydration, while the lower CRISM hydration in another area of GT does not correspond to a significantly lower DAN-derived hydration. We find that CRISM measured lower hydration in areas with rough surface texture and sand cover, while DAN bulk hydration is relatively insensitive to these characteristics. DAN active neutron results also show that the stratigraphically higher section of GT has significantly higher neutron absorption, which could be due to Fe- and Mn-rich diagenetic features. Additionally, DAN results show that GT is enriched in hydrogen with respect to other, less clay-rich units observed throughout the traverse, suggesting that subsurface clay minerals could be a significant reservoir for the hydration measured by DAN in GT.

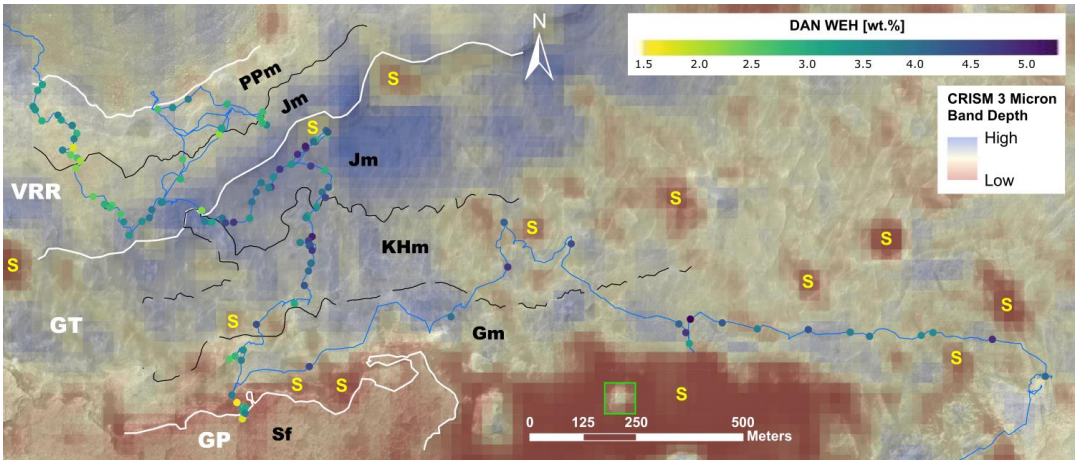

Figure 1. Map showing the study area with geomorphic features Vera Rubin ridge (VRR), Glen Torridon (GT), and Greenheugh pediment (GP) labeled in white, and geologic units (Fedo et al., 2022) "Pettegrove Point" member (PPm), "Jura" member (Jm), "Knockfarril Hill" mem- ber (KHm), "Glasgow" member (Gm), and "Stimson" formation (Sf) labeled in black (dashed where inferred). The Jura member spans the VRR-GT boundary. DAN active WEH results are symbolized along the Curiosity traverse (blue line). The basemap is a HiRISE mosaic (Calef III & Parker, 2016). A CRISM 3 μm band depth map is overlain on the HiRISE base. Several of the larger wind-blown sand patches are labeled 'S' and correspond to the lowest 3 μm areas.

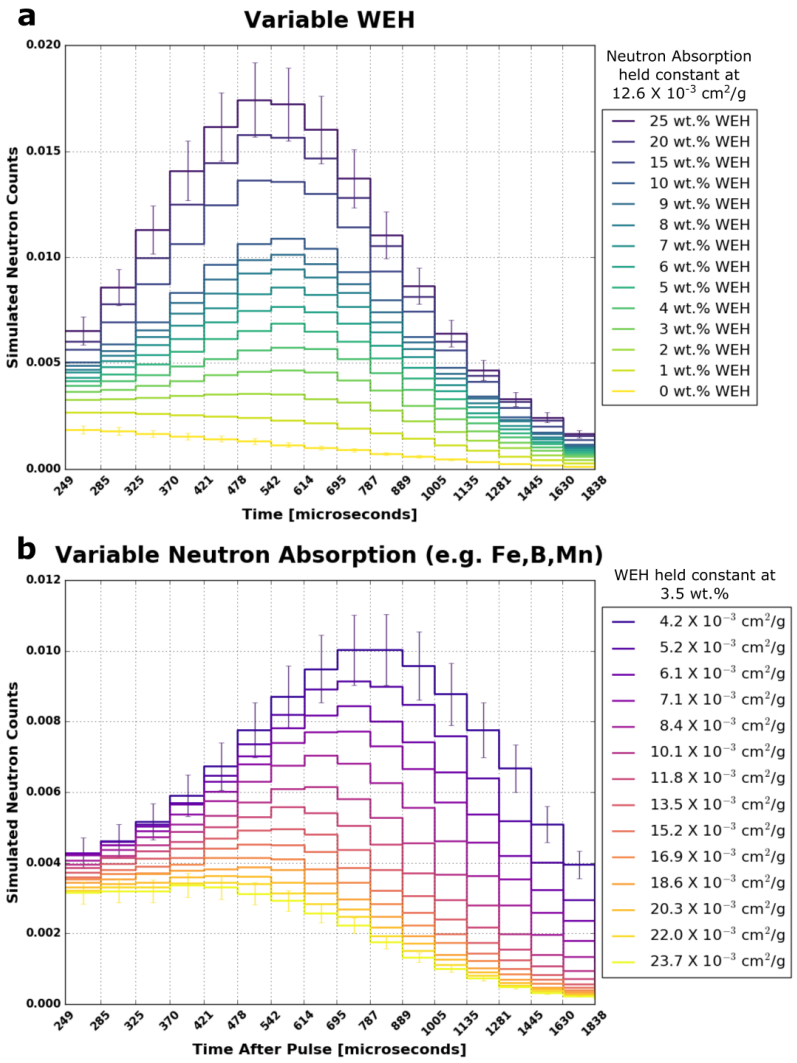

Figure 2. (a) Plot of simulated thermal neutron counts using the DAN active model geometry with set subsurface neutron absorption cross section ($12.6x10^{-3}$ cm^2/g) and variable subsur- face hydration (in water-equivalent hydrogen, WEH). (b) Plot of simulated thermal neutron counts using the DAN active model geometry with set subsurface hydration (3.5 wt.% WEH) and variable subsurface thermal neutron absorption cross section (Σabs). Statistical uncertainty error bars are shown for the top and bottom curves in each plot.

5. 河流三角洲对海平面加速上升的动态响应模型

翻译人：张靖宇 zhangjy6@sustech.edu.cn

Hariharan J, Passalacqua P, Xu Z, et al. ***Modeling the Dynamic Response of River Deltas to Sea-Level Rise Acceleration****[J]. Journal of Geophysical Research: Earth Surface, e2022JF006762.*
https://doi.org/10.1029/2022JF006762

摘要：气候变化正在不断的提高全球的海平面。在河流三角洲，海平面上升（SLR）可能导致土地流失、盐分侵入地下水蓄水层，以及对沿海单元产生不利影响的其他问题。未来海平面上升的轨迹和幅度有很大的不确定性，甚至在十年的时间尺度上也是如此。鉴于这种不确定性，需要建立数值模型来探索不同的 SLR 会如何影响河流三角洲的演变。在这项工作中，我们应用 pyDeltaRCM 数值模型模拟了三种不同的 SLR 轨迹下 350 年的三角洲演变：稳定上升、SLR 速率的突然变化和 SLR 的逐渐加速。对于每个 SLR 轨迹，除了没有 SLR 的控制运行外，我们还测试了一组 5 至 40 mm/yr 的六个最终 SLR 幅度。我们发现，地表河道动态以及地表下层的各个方面都会随着较高的 SLR 速率而发生变化，甚至在百年的时间尺度上也是如此。特别是，由于 SLR 导致的河道流动性增加，对应于地表下更高的砂连通性。SLR 变化的轨迹和幅度都会影响三角洲表面的演化，而三角洲又会改变地表下的结构。我们确定了地表和地表下属性之间的相关性，并发现，从目前的地表布局推断地表下结构应限制在海平面驱动的大致稳定的时间跨度内。因此，这项工作提高了我们在海平面持续上升时预测未来三角洲演化与地表下的连通性。

ABSTRACT: Climate change is raising sea levels across the globe. On river deltas, sea-level rise (SLR) may result in land loss, saline intrusion into groundwater aquifers, and other problems that adversely impact coastal communities. There is significant uncertainty surrounding future SLR trajectories and magnitudes, even over decadal timescales. Given this uncertainty, numerical modeling is needed to explore how different SLR projections may impact river delta evolution. In this work, we apply the pyDeltaRCM numerical model to simulate 350 years of deltaic evolution under three different SLR trajectories: steady rise, an abrupt change in SLR rate, and a gradual acceleration of SLR. For each SLR trajectory, we test a set of six final SLR magnitudes between 5

and 40 mm/yr, in addition to control runs with no SLR. We find that both surface channel dynamics as well as aspects of the subsurface change in response to higher rates of SLR, even over centennial timescales. In particular, increased channel mobility due to SLR corresponds to higher sand connectivity in the subsurface. Both the trajectory and magnitude of SLR change influence the evolution of the delta surface, which in turn modifies the structure of the subsurface. We identify correlations between surface and subsurface properties, and find that inferences of subsurface structure from the current surface configuration should be limited to time spans over which the sea level forcing is approximately steady. As a result, this work improves our ability to predict future delta evolution and subsurface connectivity as sea levels continue to rise.

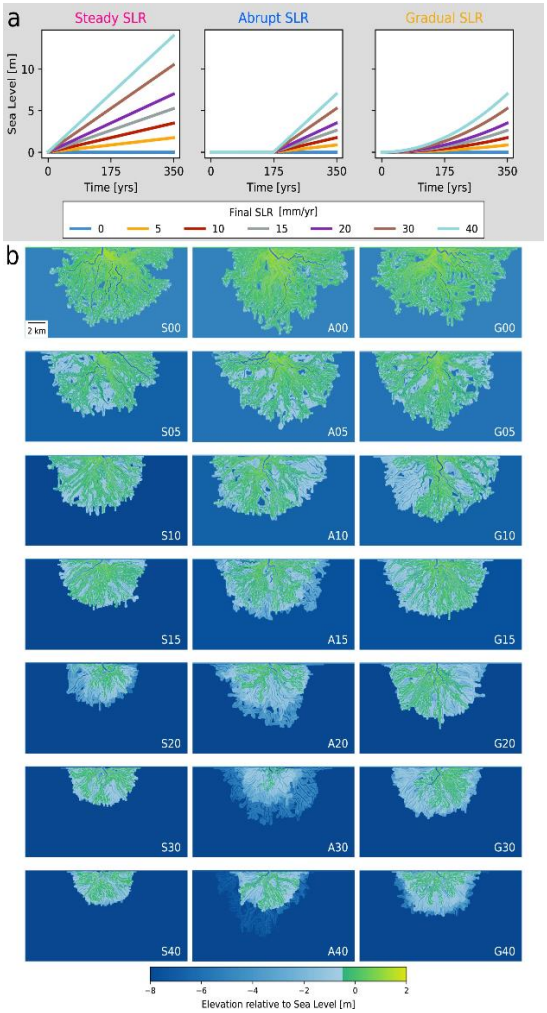

Figure 1. (a) The 21 scenarios simulated, grouped by trajectory of sea-level rise (SLR). (b) Representative final pyDeltaRCM topographies for each of the different scenarios (Table 1) with elevations shown relative to final sea levels.

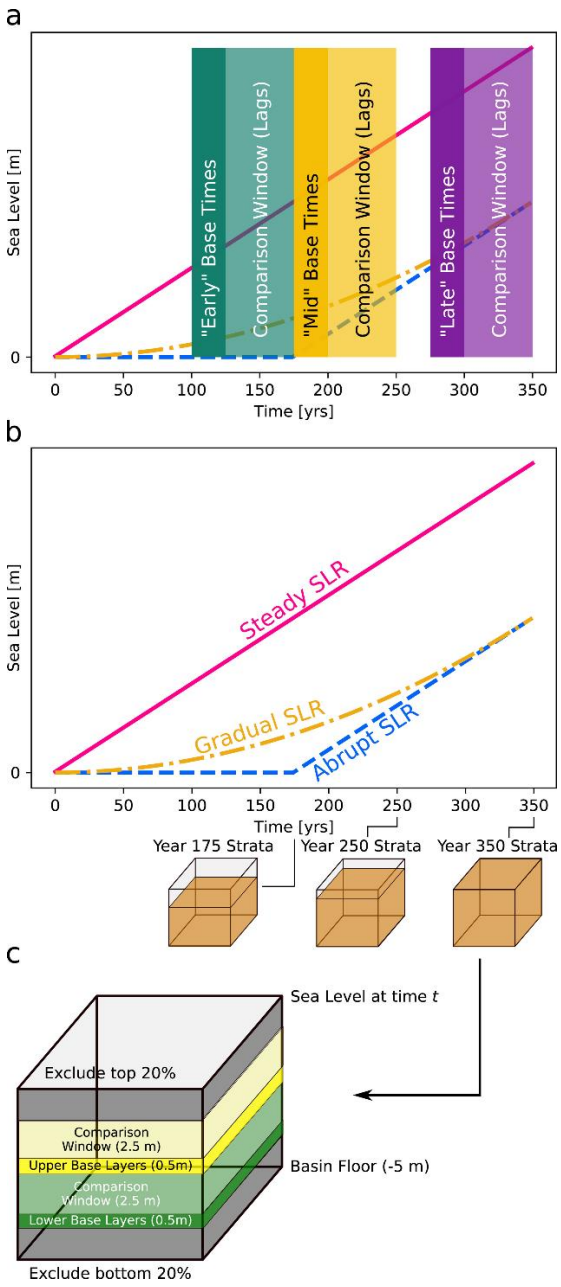

Figure 2. (a) Three analysis windows used for surface mobility computations overlaid on the generic sea level curves for the three types of scenarios. (b) The generic sea-level curves for each style of sea-level rise (SLR) with schematics of the stratigraphy cubes extracted at different points in time for the subsurface mobility analysis. (c) Schematic describing the division of the stratigraphy cube into an upper and lower section for separate analysis of the subsurface mobility; the top and bottom 20% of the deposit are omitted.

6. 四国盆地中新世半深海沉积物物源研究及其对黑潮早期历史的指示意义

翻译人：刘伟 inewway@163.com

Shi M, Wu H, Zhao X, et al. ***Provenance study of the Miocene hemipelagic sediments in the Shikoku Basin and implication for the earlier history of the Kuroshio Current****[J]. Marine Geology, 2022, 450: 106861.*

https://doi.org/10.1016/j.margeo.2022.106861

摘要：黑潮是西北太平洋最大的西边界流，对新生代气候演化和海洋环流变化起着至关重要的作用。四国盆地位于黑潮下游，其古海洋学特征对黑潮的演化十分敏感。本文利用岩石磁学、Sr 同位素组成、粒度分析和钙质微体化石研究相结合的方法，对四国盆地 IODP C0011 孔岩性单元 III 的沉积物进行了中新世半深海沉积物物源的研究。综合结果表明，~10-11 Ma 以来，单元 III 上部多畴 (钛)磁铁矿含量增加，$^{87}Sr/^{86}Sr$ 值升高(0.712 ~ 0.714)，沉积物粒度变细。磁性参数、Sr 同位素组成和粒度是沉积物源的可靠指标，基于此，将多畴(钛-)磁铁矿浓度的增加归因于来自东海的碎屑输入的增加，该碎屑富含细粒颗粒和粗粒磁铁矿，$^{87}Sr/^{86}Sr$ 比值较高(0.712～0.727)。更进一步地，增强的西部边界流（后来被称为黑潮）被认为是来自东海的细粒碎屑物通量增加的一个合理原因。我们的研究提供了一个更早的~10-11 Ma 的黑潮记录，为理解西北太平洋新生代海洋环流变化和气候演化提供了新的认识。

ABSTRACT: The Kuroshio Current (KC) is the biggest western boundary current in the northwest Pacific Ocean and plays an essential role in the Cenozoic climate evolution and ocean circulation changes. Paleoceanography of the Shikoku Basin, located downstream of the KC region, is sensitive to the evolution of the KC. In this study, the Miocene hemipelagic sediment supply in the Shikoku Basin has been investigated on sediments from lithologic Unit III of IODP Site C0011 using a combination of rock magnetism, Sr isotope composition, grain size analysis, and calcareous nannofossil study. Integrated results reveal that multidomain (MD) (titano-) magnetite concentration increases in the upper part of Unit III since ~10–11 Ma with elevated 87Sr/86Sr values (0.712–0.714) and fining up sediment grain size. Magnetic parameters, Sr isotope composition, and grain size, as reliable indicators of sediment sources, have been used to discriminate the geological sources of the sediments and attribute the increase in MD (titano-) magnetite concentration to the

increasing detrital input from the East China Sea (ECS), which is rich in fine-grained particles and coarse-grained magnetite and have high 87Sr/86Sr ratio (0.712–0.727). Furthermore, the intensified western boundary current later became known as the KC is interpreted as a plausible reason for increasing fine-grained flux from the ECS. Our study provides a much earlier record of the KC at ~10–11 Ma, giving new insight into understanding the Cenozoic ocean circulation changes and climate evolution in the northwest Pacific Ocean.

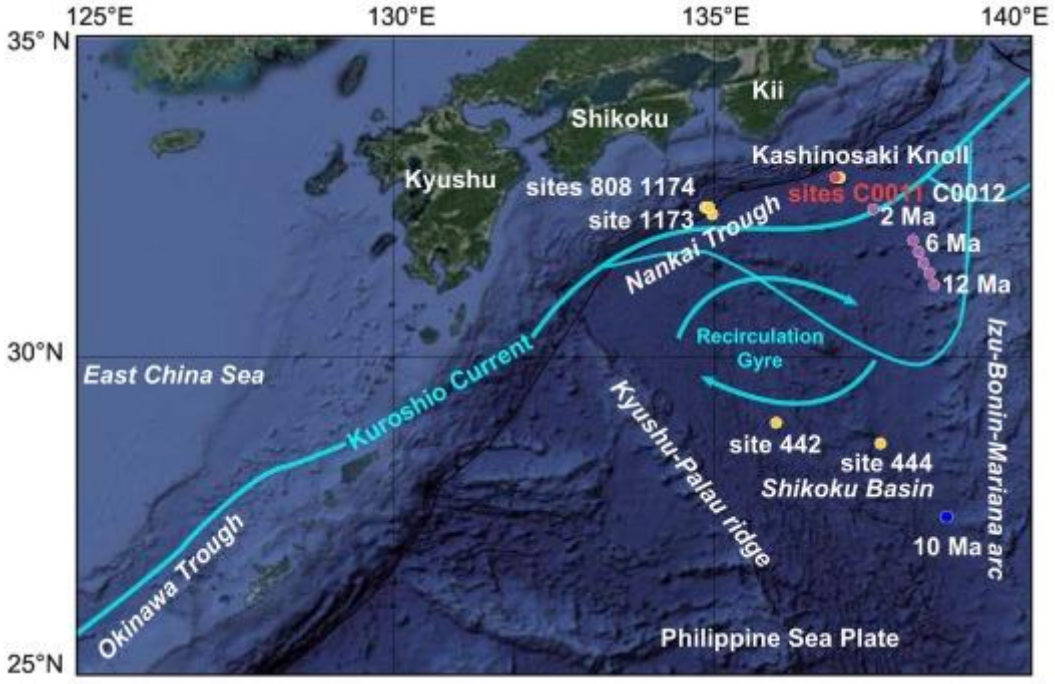

Figure 1. Map of the Shikoku Basin. Red point showing the International Ocean Discovery Program (IODP) Site C0011. Violet points showing the calculated locations of Site C0011 from ~12 Ma to present (Expedition 322 scientists, 2010). Blue point showing position of C0011 at ~10 Ma based on the plate reconstruction (Wu et al., 2016). Light yellow points showing the IODP Site C0012 (Expedition 322 scientists, 2010), ODP Sites 808, 1173 and 1174 (Shipboard Scientific Party, 1991; Shipboard Scientific Party, 2001a, Shipboard Scientific Party, 2001b).

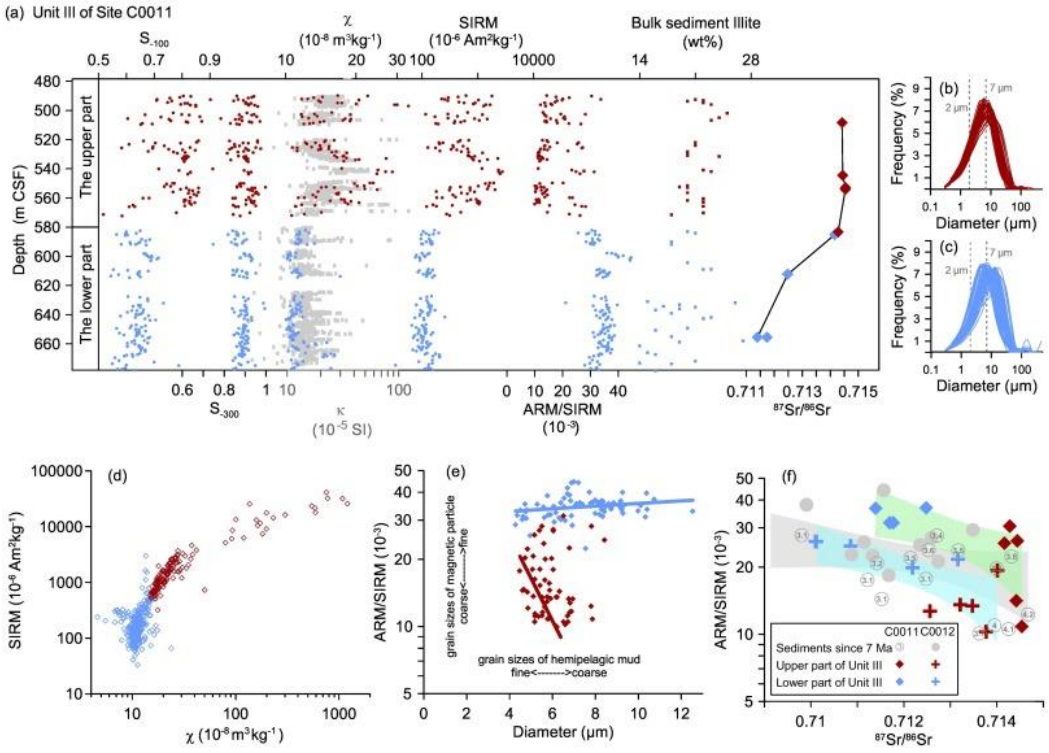

Figure 2. (a) Down-core variations of magnetic parameters for Site C0011. Magnetic composition-dependent parameter S-ratio (S-100, S-300), shipboard volume magnetic susceptibility (κ) recovered during IODP Expedition 322 (Expedition 322 scientists, 2010), magnetic concentration-dependent parameters χ and SIRM, magnetic granulometric parameter ARM/SIRM, depth profiles of illite in bulk sediment (Underwood and Guo, 2013) and 87Sr/86Sr. (b, c) Grain size analyses for the hemipelagic samples from Site C0011. (d) Cross-plots of magnetic parameters χ and SIRM. (e) Cross-plots of magnetic parameter ARM/SIRM and average diameter. (f) Cross-plots of magnetic parameter ARM/SIRM and Sr isotope composition. Rudy red and baby blue symbols representing samples from the upper part and the lower part of Unit III from Sites C0011 and C0012, respectively. 87Sr/86Sr of the upper Shikoku Basin sediments from Site C0011 between 4.2 and 3.1 Ma was obtained by Saitoh et al. (2015) showed with age. Gray symbols show samples from adjacent Site C0012 since 7 Ma. Gray, blue and green shadings indicate the 95% confidence intervals in the linear regression results of sediments since 7 Ma, sediments from Unit III of Site C0012, and sediments from Unit III of Site C0011, respectively.

7. Heinrich 5 期间亚洲夏季风多阶段演变和降雨响应

翻译人：杨会会 11849590@mail.sustech.edu.cn

Liu D B, Mi X, Liu S S , et al., ***Multi-phased ASM evolution and rainfall response during Heinrich Stadial 5 [J].*** *Research Square, 2022.*

https://doi.org/10.21203/rs.3.rs-1687308/v1

摘要：本文利用跨越 Chinese Interstadial 13（CIS13）到 Heinrich Stadial 5（HS5）的中国南方 Wulu 洞石笋的 $\delta^{18}O$ 和微量元素记录，重建了亚洲夏季风(ASM)环流和区域降水的变化。在 HS 5 期间急于石笋 $\delta^{18}O$ 变化的 ASM 的演变可分为 4 个阶段，即突然开始/终止和 HS 5 中期的不稳定阶段(ASM 缓慢减弱，之后逐步增强)。相对于 $\delta^{18}O$ 的平均值，ASM 在 HS 5 中期阶段的减弱程度，达到 HS 5 总变化量级的 58%。相反，基于微量元素推断的降雨变化的多阶段变化并不清楚，表现为冰阶-间冰阶模式。在 CIS 13 期间，大幅度的元素振荡伴随着 HS 5 开始时的快速下降，而在 HS 5 中的变幅有限。与平均水平相比，HS 5 中期的降水减少约为整个事件的 33%，与 Chinese Stadial 14 的降水量相当。这表明，ASM 对 HS 5 具有明显的敏感性，而降雨对 HS 5 的响应存在延迟。HS 5 期间，热带太平洋东部降温有利于 La Niña 状态的形成和华南的湿润。我们记录的 HS 5 发生的时间(48.53±0.12 ka, 47.19±0.12 ka)与广大空间内的其他洞穴记录的中心年龄(48.72±0.14 ka, 47.35±0.24 ka)吻合较好。在 HS5 开始时，亚洲水文气候变化与两极冰芯记录同期，但在结束时领先格陵兰岛暖化约 300 年，或与以大气 CH_4 约束年龄的格陵兰记录同期。这至少表明，在 HS5 期间，季风降水对气候扰动的敏感性较低。

ABSTRACT: Changes in Asian summer monsoon (ASM) circulation and regional precipitation were reconstructed from stalagmite $\delta^{18}O$ and trace element records from Wulu Cave in southern China, covering Chinese Interstadial (CIS) 13 to Heinrich Stadial (HS) 5. During HS 5, the evolution of $\delta^{18}O$ -based ASM can be divided into four stages, i.e., an abrupt onset/termination and unstable mid-HS 5 (a slow ASM decline followed by a stepwise ASM strengthening). The extent of ASM weakening in mid-HS 5, relative to the mean $\delta^{18}O$ value, reaches 58% of the total magnitude of HS

5. In contrast, multi-stage variability is less clear in element-inferred rainfall variations, which feature a stadial/interstadial pattern. During CIS 13, large-amplitude element oscillations are accompanied by a rapid decline at the onset of HS 5, with a limited range of variability in HS 5. The rainfall reduction in mid-HS 5, in comparison with the mean level, approximates 33% of the full event, practically equivalent to that during Chinese Stadial (CS) 14. It suggests a pronounced sensitivity of ASM and an inertial precipitation response to HSs. During HS 5, a cooling in the eastern tropical Pacific could favor a formation of La Niña state and a wetting in southern China. The timing of HS 5 in our record (48.53±0.12 ka, 47.19±0.12 ka) agrees well with the central age of spatially-separated cave records (48.72±0.14 ka, 47.35±0.24 ka). At the onset of HS 5, Asian hydroclimate changes are coeval with bipolar ice-core records, but lead the Greenland warming by 300 years at the termination or are synchronous with Greenland records via atmospheric CH_4 constraints. This at least implicates that the monsoonal rainfall is less sensitive to climate perturbations during HS 5.

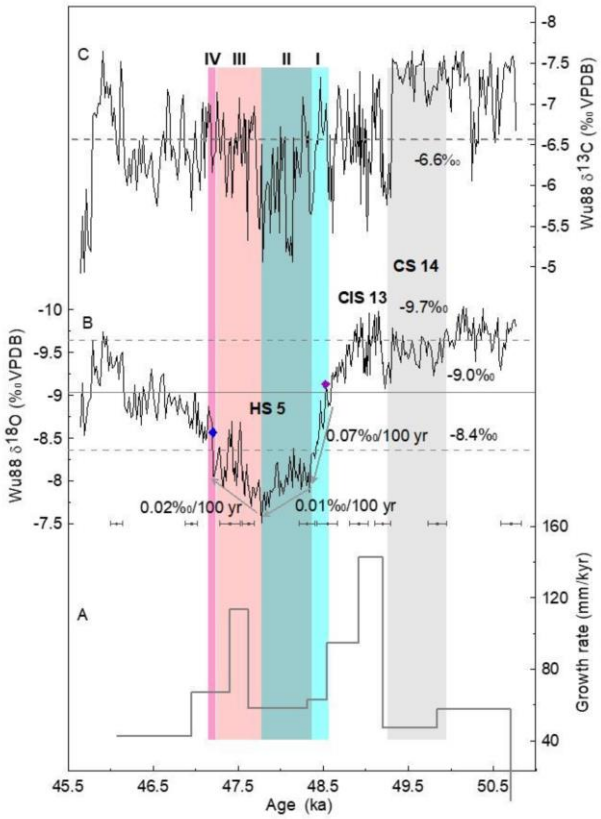

Figure 1. Isotopic and growth rate records of sample Wu88. (A) growth rate, (B) $\delta^{18}O$, (C) $\delta^{13}C$. Gray and color bars indicate CS 14 and four stages of HS 5 following the $\delta^{18}O$ record, respectively. Dashed

line in Figure C depicts the mean value of $\delta^{13}C$ record, while solid and dashed lines in Figure B denote the mean value and one standard deviation, with dating results and errors shown below. Purple and blue diamonds illustrate the onset and end of HS 5. Arrowed lines display multi-phased ASM variability in HS 5.

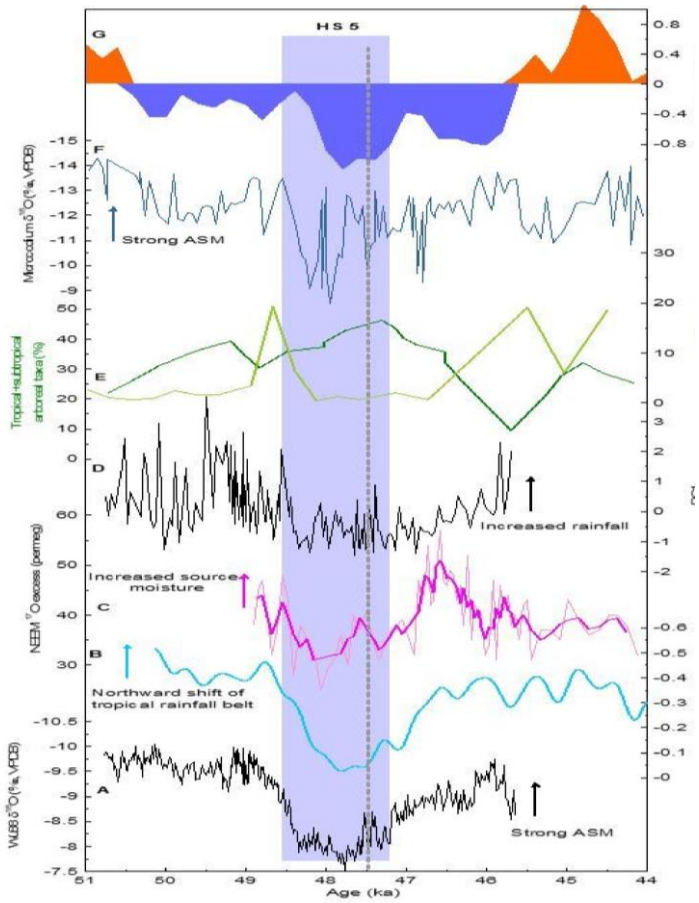

Figure 2. Dynamical link of Asian hydroclimate and other geologic records. (A) Wu88 $\delta^{18}O$ record, (B) atmospheric $\delta^{18}O$ inferred fractionation changes by the global terrestrial biosphere ($\Delta_{\varepsilon LAND}$), representing a latitudinal shift of tropical rainfall (Seltzer et al., 2017), (C) NEEM ^{17}O excess, a proxy for low-latitude hydrological cycle (Guillevic et al., 2014). Bold pink line: three-year running average. (D) Wu88 elemental PC1 record, (E) concentrations of tropical and subtropical arboreal taxa (dark green) and bilobate phytoliths (light green) (Zhang et al., 2020), (F) microcodium $\delta^{18}O$ record from the southeastern Loess Plateau (Zhang et al., 2022), and (G) sea surface difference between western and eastern tropical Pacific (Data source from Supplementary Fig. 6). The blue bar displayed HS 5, and the dotted line depicted ASM rise in late HS 5.

8. 在白垩纪中期大洋缺氧事件 1b（Aptian-Albian 过渡）期间，轨道周期的全球海洋脱氧与火山 CO_2 排放脱钩

翻译人：曹伟 11930854@qq.com

Wang, Y, Bodin, S, Blusztajn, J S. ***Orbitally paced global oceanic deoxygenation decoupled from volcanic CO_2 emission during the middle Cretaceous Oceanic Anoxic Event 1b (Aptian-Albian transition)*** *[J].* ***Geology****, 2022.*

https://doi.org/10.1130/G50553.1

摘要：持续的海洋氧气缺失将对地球上生命的分布和密度产生深远影响。然而，目前对全球海洋脱氧起始和终止的驱动因素知之甚少。在此，我们提出了一个铊同位素记录，揭示了白垩纪中期三个快速(50 k.y)的全球脱氧间隔期，这些时间至少晚于大规模火山活动 1 m.y。新的锶同位素数据显示，在火山活动之后，气候变暖，大陆风化逐渐增强。然而，只有在气候变暖的长期风化率增加和导致大气环流重组的短期轨道调谐的共同影响下全球脱氧才会发生。多个驱动的交互作用与各脱氧区间的突然终止是一致的。白垩纪中期的动态氧化反应强调了这些过程对理解当前海洋脱氧的后果和潜在终止的作用。

ABSTRACT: The ongoing oceanic oxygen loss will have a profound impact on the distribution and density of life on Earth. However, drivers of the initiation and termination of global oceanic deoxygenation are poorly understood. Here we present a thallium isotope record that reveals three rapid (50 k.y.) global deoxygenation intervals during the mid-Cretaceous that postdate massive volcanism by at least 1 m.y. New strontium isotope data reveal gradually enhanced continental weathering under a warmer climate following volcanism. However, global deoxygenation occurred only under the combined influences of a long-term increase in weathering rates in a warmer climate and short-term orbital modulation that led to atmospheric-circulation reorganization. Interactions of multiple drivers are consistent with the abrupt termination of each deoxygenation interval. Dynamic oxygenation responses in the mid-Cretaceous highlight the role of these processes for understanding the consequences and potential termination of the current oceanic deoxygenation.

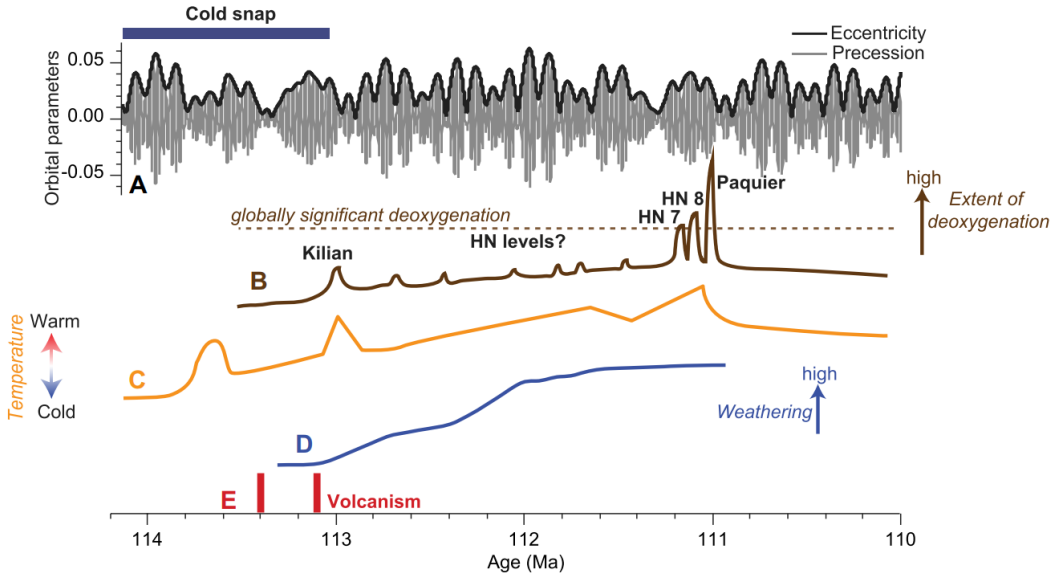

Figure 1. Forcing mechanisms of oceanic oxygenation changes in Oceanic Anoxic Event (OAE) 1b. (A) Orbital parameters (Laskar et al., 2004). Eccentricity is in black and precession in gray. (B) Qualitatively estimated extent of deoxygenation is based on shale deposition and ε^{205}Tl records of the Briers section. HN horizon noir levels. (C) Nannofossil-based temperature reconstructions (Bottini and Erba, 2018). (D) Weathering fluxes from $^{87}Sr/^{86}Sr$ in Figure 3. (E) Volcanism from Os isotopes (Matsumoto et al., 2020). Magnitude of volcanism is not to scale.

9. 南半球高纬度地区晚白垩世大洋缺氧事件 2 期间的生物和古海洋学变化---基于印度洋东南部 IODP U1513 和 U1516 站位的研究

翻译人：王浩森 11930841@mail.sustech.edu.cn

Petrizzo M R, Amaglio G, Watkins D K, et al. ***Biotic and paleoceanographic changes across the Late Cretaceous Oceanic Anoxic Event 2 in the southern high latitudes (IODP Sites U1513 and U1516, SE Indian Ocean)****[J]. Paleoceanography and Paleoclimatology, e2022PA004474.*

https://doi.org/10.1029/2022PA004474

摘要：跨越 Cenomanian/Turonian 边界（93.9 Ma）的大洋缺氧事件 OAE 2 是重要的全球碳循环扰动事件。为了调查对生物群的响应和整个事件中的古海洋学条件，我们分析了来自国际海洋发现计划 U1513 和 U1516 钻孔的数据，这些地点位于门特尔盆地（澳大利亚西南部近海；白垩纪中期的古纬度为 59 °–60 °S），记录了南半球高纬度地区 OAE 2 的首次完整记录。钙质超微化石提供了可靠的生物年代地层框架。浮游和底栖有孔虫、放射虫和钙球的分布和丰度模式能够解释水团分层的动力学，并为两个地点的古水深重建提供支持，U1513 位于曼特尔盆地沉积中心西北部，深度比 U1516 地点更深。下 OAE 2 层段的特点是水团分层减少，地表水生产力交替增强，混合层厚度变化，如居中浮游有孔虫丰度波动所示。中部 OAE 2 层段包含几乎完全由放射虫组成的岩性，反映了极高的海洋生产力；低 $CaCO_3$ 含量与碳酸盐补偿深度明显变浅以及由于 $CaCO_3$ 欠饱和导致的海洋酸化一致。微化石变化反映了富硅、贫碳酸钙岩石沉积后的条件缓和，表明相对稳定的水柱。

ABSTRACT: Oceanic Anoxic Event 2, spanning the Cenomanian/Turonian boundary (93.9 Ma), was an episode of major perturbations in the global carbon cycle. To investigate the response of biota and the paleoceanographic conditions across this event, we present data from International Ocean Discovery Program sites U1513 and U1516 in the Mentelle Basin (offshore SW Australia; paleolatitude 59°–60°S in the mid-Cretaceous) that register the first complete records of OAE 2 at southern high latitudes. Calcareous nannofossils provide a reliable bio-chronostratigraphic framework. The distribution and abundance patterns of planktonic and benthic foraminifera, radiolaria, and calcispheres permit interpretation of the dynamics of the water mass stratification and provide support for the paleobathymetric reconstruction of the two sites, with Site U1513

located northwest of the Mentelle Basin depocenter and at a deeper depth than Site U1516. The lower OAE 2 interval is characterized by reduced water mass stratification with alternating episodes of enhanced surface water productivity and variations of the thickness of the mixed layer as indicated by the fluctuations in abundance of the intermediate dwelling planktonic foraminifera. The middle OAE 2 interval contains lithologies composed almost entirely of radiolaria reflecting extremely high marine productivity; the low $CaCO_3$ content is consistent with marked shoaling of the Carbonate Compensation Depth and ocean acidification because of $CaCO_3$ undersaturation. Conditions moderated after deposition of the silica-rich, $CaCO_3$-poor rocks as reflected by the microfossil changes indicating a relatively stable water column although episodes of enhanced eutrophy did continue into the lower Turonian at Site U1516.

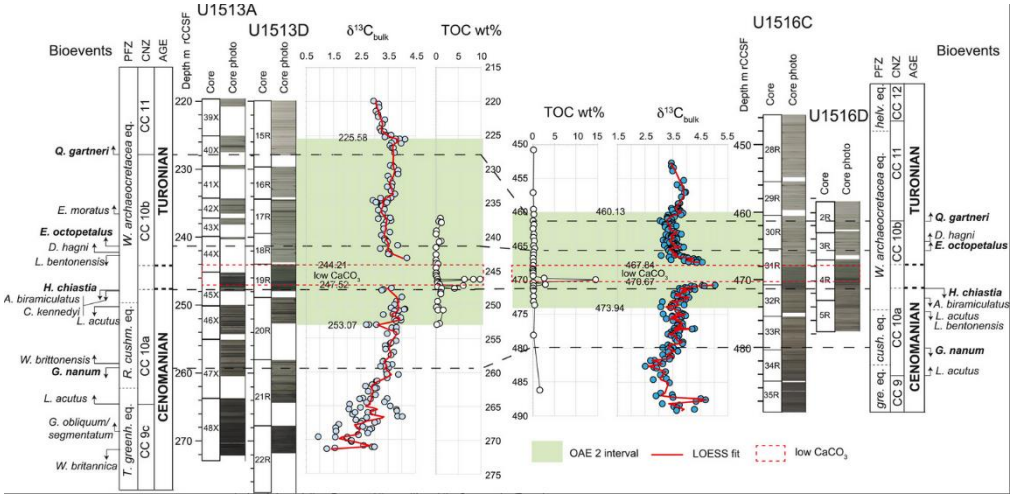

Figure 1. Stratigraphic correlation between sites U1513 and U1516. Site U1513: core recovery and core photo from Huber et al. (2019a); planktonic foraminifera and calcareous nannofossil biostratigraphy, age, carbon isotope bulk carbonate, interval of low $CaCO_3$ content and total organic carbon (TOC) according to this study (see Figure 2). Site U1516: data are from Petrizzo et al. (2021) except planktonic foraminifera Zones and the position of the Cenomanian/Turonian boundary that have been revised in this study (see text for explanation). For the identification of the OAE 2 interval (light green band) see explanation in the text. Abbreviations: m rCCSF = revised Core Composite depth below Sea Floor in meters; PFZ = Planktonic Foraminifera Zones; CNZ = Calcareous Nannofossils Zones; *helv*. eq = *Helvetoglobotruncana helvetica* equivalent; *W*. *archaeocretacea* eq. = *Whiteinella archaeocretacea* equivalent; *R*. *cushm*. eq., *cush*. eq. = *Rotalipora cushmani* equivalent; *T*. *greenh*. eq., *gre*. eq. = *Thalmanninella greenhornensis* equivalent.

10. 大西洋-北极洋口水深变化对始新世-渐新世气候转变的影响

翻译人：王敦繁 Dunfan-w@foxmail.com

Straume, E, Nummelin, A, Gaina, C,et al. 2022, ***Climate transition at the Eocene–Oligocene influenced by bathymetric changes to the Atlantic–Arctic oceanic gateways*** *[J], PNAS, 17, 2022, e2115346119.*
https://doi.org/10.1073/pnas.2115346119

摘要：始新世-渐新世过渡(~ 33.9 Ma)标志着新生代降温趋势中最大的阶跃转变，其特征是南极冰盖的突然增长、内部海洋的冷却和强烈的经向温度梯度的建立。在这里，我们通过在最先进的地球系统模型(挪威地球系统模型[NorESM-F])中对大西洋-北极盆地的真实古海底模型进行详细的古地理重建，研究始新世-渐新世过渡时期海洋入口变化的气候影响。我们证明，温暖的始新世气候对格陵兰-苏格兰岭和原始弗拉姆海峡的深度变化高度敏感，因为它们控制着淡水从北极向北大西洋的泄漏。我们的研究结果和代理证据表明，这些通道的变化控制着海洋环流，并在陆基冰盖的增长中发挥了关键作用，此外还有二氧化碳驱动的全球变冷。具体地说，我们认为北极和北大西洋之间的浅连接在晚始新世限制了新鲜地表水向南流动，形成了北大西洋翻转环流。因此，南半球的温度下降了几度，为南极洲的冰川作用铺平了道路。不久之后，由于冰岛地幔柱的动力支持减弱，与北极的联系加深了。这削弱了北大西洋的翻转，使北半球变冷，从而促进了那里的冰川作用。我们的研究指出，东北大西洋通道和大气 CO_2 的减少在两个半球冰川的发生中起着控制作用。

ABSTRACT: The Eocene–Oligocene Transition (~33.9 Ma) marks the largest step transformation within the Cenozoic cooling trend and is characterized by a sudden growth of the Antarctic ice sheets, cooling of the interior ocean, and the establishment of strong meridional temperature gradients. Here we examine the climatic impact of oceanic gateway changes at the Eocene–Oligocene Transition by implementing detailed paleogeographic reconstructions with realistic paleobathymetric models for the Atlantic–Arctic basins in a state-of-the-art earth system model (the Norwegian Earth System Model [NorESM-F]). We demonstrate that the warm Eocene climate is highly sensitive to depth variations of the Greenland–Scotland Ridge and the proto–Fram Strait as they control the freshwater leakage from the Arctic to the North Atlantic. Our results, and proxy

evidence, suggest that changes in these gateways controlled the ocean circulation and played a critical role in the growth of land-based ice sheets, alongside CO2-driven global cooling. Specifically, we suggest that a shallow connection between the Arctic and North Atlantic restricted the southward flow of fresh surface waters during the Late Eocene allowing for a North Atlantic overturning circulation. Consequently, the Southern Hemisphere cooled by several degrees paving the way for the glaciation of Antarctica. Shortly after, the connection to the Arctic deepened due to weakening dynamic support from the Iceland Mantle Plume. This weakened the North Atlantic overturning and cooled the Northern Hemisphere, thereby promoting glaciations there. Our study points to a controlling role of the Northeast Atlantic gateways and decreasing atmospheric CO2 in the onset of glaciations in both hemispheres.

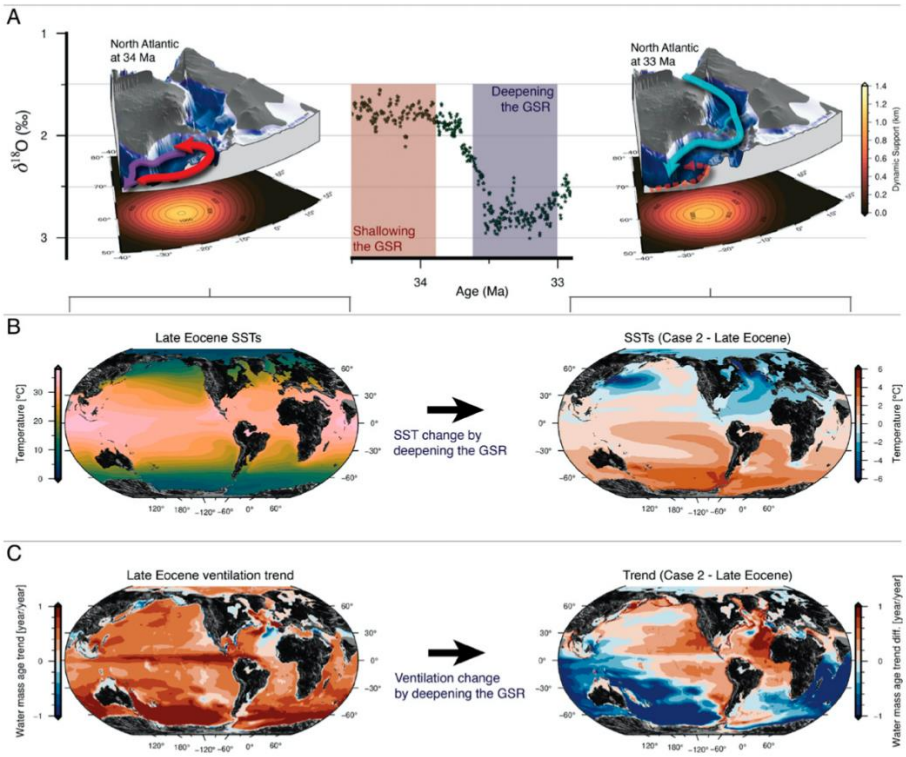

Figure 1. Changes in Iceland mantle plume activity leading to changes in SSTs and ocean ventilation. (A) The benthic oxygen isotope values ($\delta^{18}O$) across the EOT and the paleogeographic configuration for 34 Ma (Left) and 33 Ma (Right), with the dynamic support from the Iceland plume and sketched ocean circulation for the respective gateway configurations based on this study. (B) The change in SSTs forms as a result of deepening the GSR (a likely paleogeo- graphic change from 34 to 33 Ma). (C) Change in ocean ventilation is measured as the trend in the vertical mean water mass age when deepening the GSR.

11. 通过 InSight 地震与声波数据对火星上新形成的撞击坑定位

翻译人：张伟杰 12031188@mail.sustech.edu.cn

Garcia R F, Daubar I J, Beucler É, et al. ***Newly formed craters on Mars located using seismic and acoustic wave data from InSight****[J]. Nature Geoscience, 2022: 1-7.*

https://doi.org/10.1038/s41561-022-01014-0

摘要：流星撞击在行星表面形成撞击坑同时改变其大气成分。在进入大气和撞击地面的过程中，流星激发瞬态声波和地震波。然而，新的陨石坑形成及相关撞击引起的机械波还没有在地球之外被同时观测到。本文，我们报告了从 NASA 洞察号着陆器的地震仪观测到的地震波和声波，我们将其与轨道拍摄的图像观测到的火星上的四个流星撞击事件联系起来。陨石坑的尺寸和估计的流星轨迹与记录的地震图的波形建模一致。有了确定的震源，地震波可以用来约束火星内部的结构，证实以前的地壳结构模型，并约束火星上冲击产生的地震波的距离和振幅之间的比例关系，支持冲击地震力矩和垂直冲击动量之间的联系。我们的发现证明了行星地震学识别撞击产生的震源和约束撞击过程和行星内部的能力。

ABSTRACT: Meteoroid impacts shape planetary surfaces by forming new craters and alter atmospheric composition. During atmospheric entry and impact on the ground, meteoroids excite transient acoustic and seismic waves. However, new crater formation and the associated impact-induced mechanical waves have yet to be observed jointly beyond Earth. Here we report observations of seismic and acoustic waves from the NASA InSight lander's seismometer that we link to four meteoroid impact events on Mars observed in spacecraft imagery. We analysed arrival times and polarization of seismic and acoustic waves to estimate impact locations, which were subsequently confirmed by orbital imaging of the associated craters. Crater dimensions and estimates of meteoroid trajectories are consistent with waveform modelling of the recorded seismograms. With identified seismic sources, the seismic waves can be used to constrain the structure of the Martian interior, corroborating previous crustal structure models, and constrain scaling relationships between the distance and amplitude of impact-generated seismic waves on Mars, supporting a link between the seismic moment of impacts and the vertical impactor

momentum. Our findings demonstrate the capability of planetary seismology to identify impact-generated seismic sources and constrain both impact processes and planetary interiors.

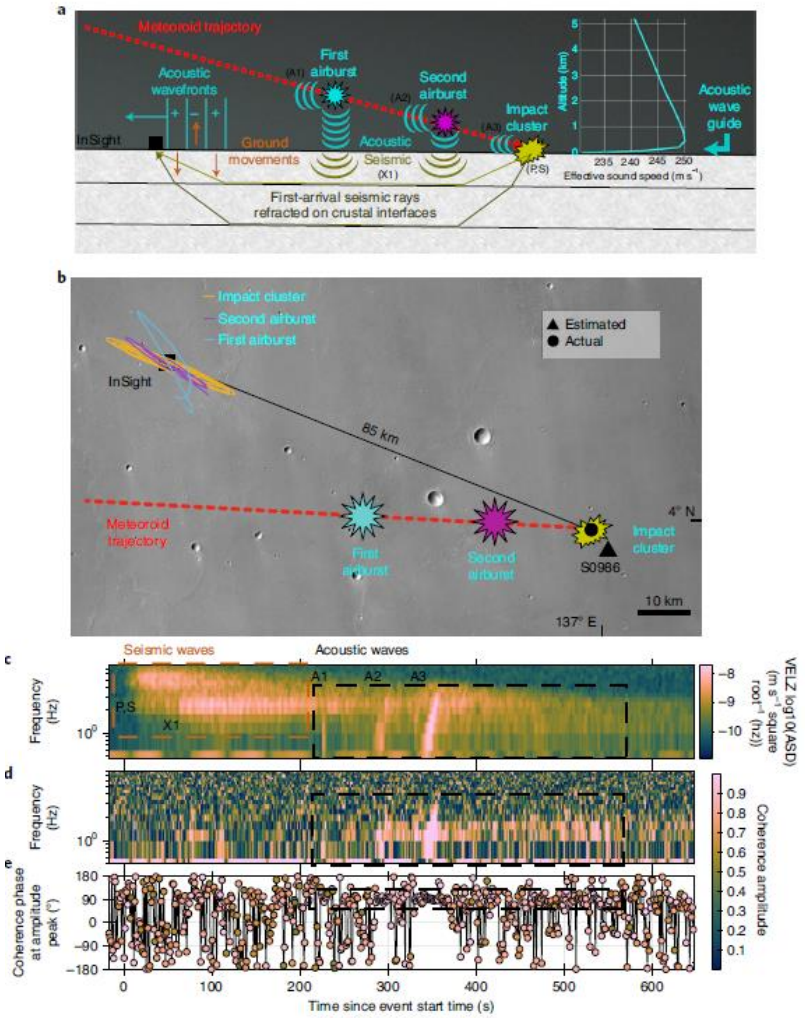

Figure 1. Sketch of meteor impact phenomena and their recordings by InSight. a, Sketch of physical processes during meteoroid entry and impact, and effective sound speed profile from impact direction to InSight extracted from MCD. Labels in parentheses locate the sources of the main acoustic and seismic arrivals. Figure is not to scale. b, Impact location and estimated meteoroid entry path on CTX mosaic background. Polarization of main acoustic signals is depicted at InSight location. c, Spectrogram of vertical component of ground velocity (VELZ) for S0986c seismic event, showing the three main seismic arrivals (P, S, X1) and the three main acoustic arrivals (A1, A2, A3). P, S and A3 are associated with the impact source; X1, A1 and A2 are associated with the two airbursts. Signal energy is provided in Amplitude Spectral Density (ASD). d, Coherence as a function of time and frequency. e, Phase relation between vertical and horizontal ground velocities at maximum coherence value. Times are provided relative to event start time(5 September 2021, 05:23:58.00 utc).

12. 全新世 ENSO 频率增强驱动安第斯山脉森林扰动

翻译人：李海 12031330@mail.sustech.edu.cn

Hagemans K, Urrego D H, Gosling W D, et al. ***Intensification of ENSO frequency drives forest disturbance in the andes during the holocene*** *[J]. Quaternary Science Reviews, 2022, 294, 107762..*

https://doi.org/10.1016/j.quascirev.2022.107762

摘要：现今，热带安第斯山脉的生物多样性山地森林经常受到降雨驱动的大规模运移的干扰，这些运动主要发生在极端厄尔尼诺事件期间。在接下来的几十年里，在 1.5°C 的全球变暖情景下，这些事件预计将翻一番。随之而来的降雨量增加和大规模运移事件可能会给生活在安第斯山脉的数百万人带来更高的风险。然而，由于缺乏将厄尔尼诺-南方涛动（ENSO）频率的过去变化与森林和景观干扰模式直接联系起来的研究，更频繁的极端降雨的影响仍不清楚。在这里，作者展示了厄瓜多尔南部拉古纳 Pallcacocha 的第一个全新世古生态记录，该地区是厄尔尼诺重建的关键地点。结果证明，在过去的 10000 年中，指示重新迁殖的植物分类群（例如 Alnus acuminata）与厄尔尼诺现象引起的湖泊洪水层共存。在晚全新世，森林扰动模式被放大，表明森林砍伐后坡面不稳定性增强。时间模式不能用树木线波动或人类影响来解释，而后者确实放大了 ENSO 对景观扰动的影响。现代 ENSO 与降水之间的空间相关性与全新世景观扰动记录的区域比较一致。作者的研究结果表明，极端气候，例如与未来厄尔尼诺现象的加剧有关的极端气候，加上持续的土地利用变化，将增加大规模移动的频率，增加安第斯山脉数百万人的居住风险。

ABSTRACT: The biodiverse montane forests of the tropical Andes are today frequently disturbed by rainfall-driven mass movements which occur mostly during extreme El Niño events. Over the coming decades these events are projected to double under the 1.5 °C global warming scenario. The consequent increased rainfall and mass movement events likely present an elevated risk to millions of people living in the Andes. However, the impact of more frequent rainfall extremes remains unclear due to a lack of studies that directly link past changes in El Niño-Southern Oscillation (ENSO) frequency to forest and landscape disturbance patterns. Here, we present the first Holocene palaeoecological record from Laguna Pallcacocha, southern Ecuador, a key site for El Niño

reconstructions. We demonstrate that for the past 10,000 years plant taxa indicative of recolonization – such as Alnus acuminata – covary with El Niño-induced flood layers in the lake. An amplified forest disturbance pattern is observed in the late Holocene, suggesting enhanced slope instability following deforestation. The temporal pattern is not explained by tree line fluctuations or human impact, while the latter does amplify the impact of ENSO on landscape disturbance. Spatial correlations between modern ENSO and precipitation are consistent with a regional comparison of Holocene records of landscape disturbance. Our results indicate that climate extremes, such as those associated with future intensification of El Niño, combined with ongoing land use change will increase the frequency of mass movements elevating risks for millions of people in the Andes.

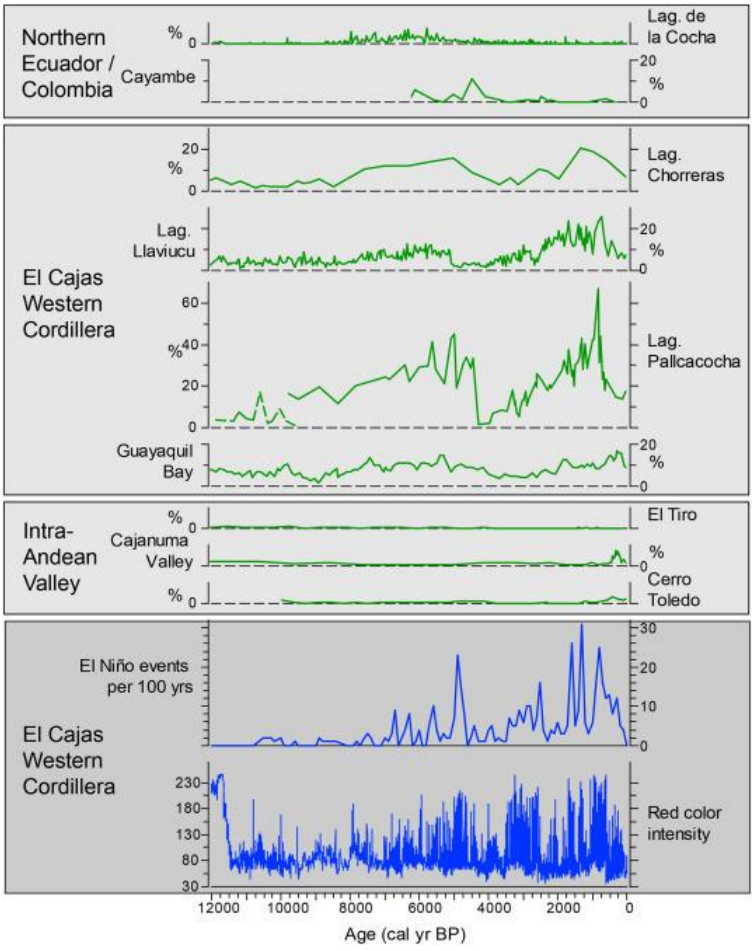

Figure 1. High elevation sites included in the regional analysis (details see Table 1). Overlay shows correlation between November–January averaged precipitation and the NINO 1.2 index 1979–2019 for Ecuador and Southern Colombia. Correlation obtained with KNMI Climate Explorer (https://climexp.knmi.nl/start.cgi) and adjusted in ArcGis (Environmental Systems Research Institute, 2014).

13. MIS 4 时期的多种碳循环机制

翻译人：张亚南 zhangyn3@mail.sustech.edu.cn

Menking J A, Shackleton S A, Bauska T K, et al. ***Multiple carbon cycle mechanisms associated with the glaciation of Marine Isotope Stage 4*** *[J] Nature Communications, 2022, 13, 5443.*
https://doi.org/10.1038/s41467-022-33166-3

摘要：本文通过高精度碳同位素数据（$\delta^{13}C\text{-}CO_2$）展示出在 MIS 4 时期（~70.5-59 ka），大气 CO_2 受到一系列千年尺度过程的控制。冰川高峰期 $\delta^{13}C\text{-}CO_2$ 的富集表明海洋碳库的增加。MIS 4 早期（~70.5-59 ka）$\delta^{13}C\text{-}CO_2$ 的变化表明，在 CO_2 下降过程中存在多种活跃过程，可能包括陆地碳库和南大洋海气交换的减少叠加在海洋碳库的增加上。MIS 4 时期维持低 CO_2 水平，而 $\delta^{13}C\text{-}CO_2$ 表现波动，这表明南大洋和北大西洋海气交换的影响。Dansgaard-Oeschger 19 事件（72.1 ka）开始时 CO_2 增加了 7ppm 以及 MIS4 晚期（HS 6, ~63.5-60 ka）大气 CO_2 增加了 27ppm，与大气中轻碳的增加有关。陆地生物圈和南大洋海气交换可能是造成这一现象的原因，后者也涉及到海洋碳库的减少。

ABSTRACT: Here we use high-precision carbon isotope data ($\delta^{13}C\text{-}CO_2$) to show atmospheric CO_2 during Marine Isotope Stage 4 (MIS 4, ~70.5-59 ka) was controlled by a succession of millennial-scale processes. Enriched $\delta^{13}C\text{-}CO_2$ during peak glaciation suggests increased ocean carbon storage. Variations in $\delta^{13}C\text{-}CO_2$ in early MIS 4 suggest multiple processes were active during CO_2 drawdown, potentially including decreased land carbon and decreased Southern Ocean air-sea gas exchange superposed on increased ocean carbon storage. CO_2 remained low during MIS 4 while $\delta^{13}C\text{-}CO_2$ fluctuations suggest changes in Southern Ocean and North Atlantic air-sea gas exchange. A 7 ppm increase in CO_2 at the onset of Dansgaard-Oeschger event 19 (72.1 ka) and 27 ppm increase in CO_2 during late MIS 4 (Heinrich Stadial 6, ~63.5-60 ka) involved additions of isotopically light carbon to the atmosphere. The terrestrial biosphere and Southern Ocean air-sea gas exchange are possible sources, with the latter event also involving decreased ocean carbon storage.

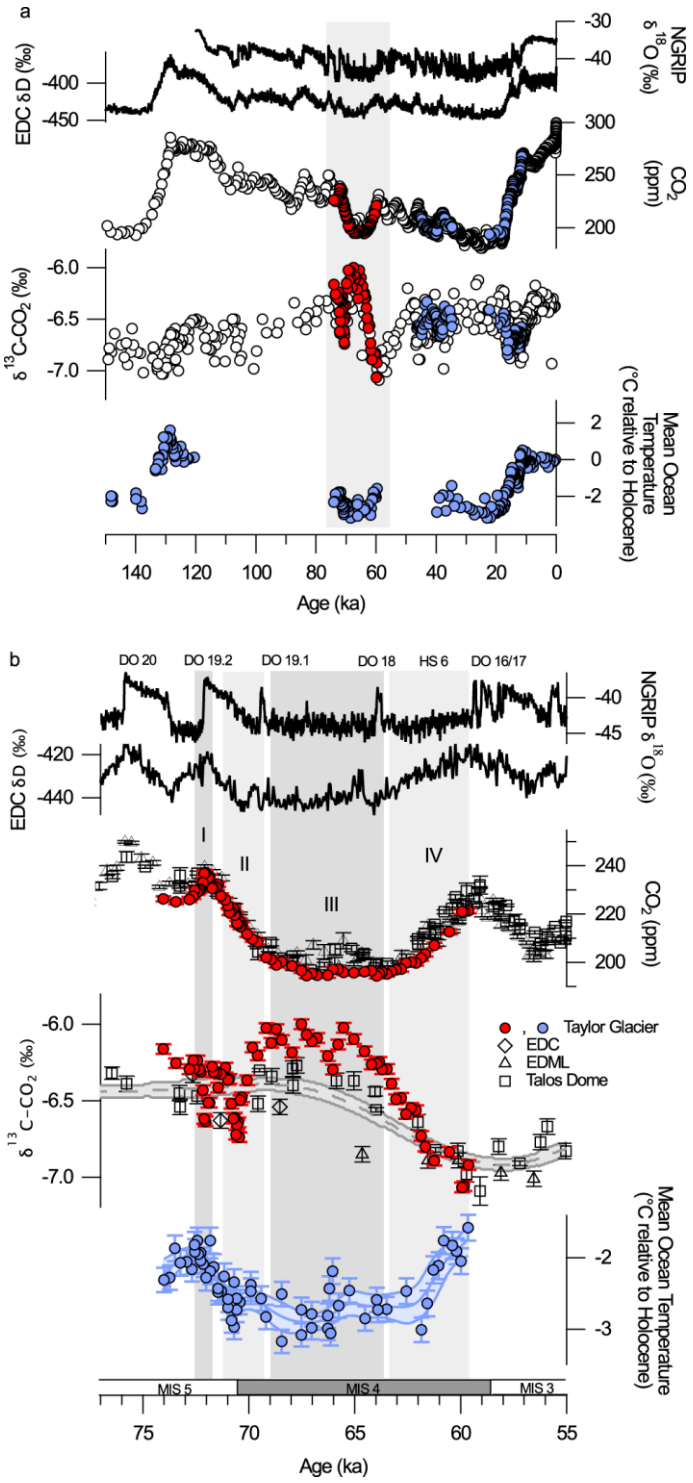

Figure 1. High-resolution CO_2 and $\delta^{13}C$-CO_2 data from Taylor Glacier. a Data from this study (red circles) show larger variations in $\delta^{13}C$-CO_2 across the transition into and out of Marine Isotope Stage 4 (74–59.5 ka) than preexisting $\delta^{13}C$-CO_2 data (white and blue circles) spanning the last two deglaciations (140–125 and 21–11 ka) and the Heinrich Stadial (HS)-4/Dansgaard–Oeschger (DO)-8 transition (46–36 ka). The large changes in the $\delta^{13}C$-CO_2 are surprising given the relatively smaller magnitude changes in CO_2. Mean ocean temperature data derived from ice core noble gas measurements show relatively smaller changes across the MIS 5-4 transition relative to the last two deglaciations. North Greenland Ice Core Project (NGRIP) and EPICA Dome C (EDC) water

isotopes are plotted for chronological and climatic reference. b An enlarged plot of the interval 77–55 ka compares Taylor Glacier data to preexisting CO2 and $\delta^{13}C$-CO_2 data from EPICA Dome C (EDC), EPICA Dronning Maud Land (EDML), and Talos Dome ice cores. The interval is divided into four subintervals (I – IV) highlighting distinct modes of change in CO_2 and $\delta^{13}C$-CO_2 discussed in the text. Error bars represent 1-sigma analytical uncertainty..

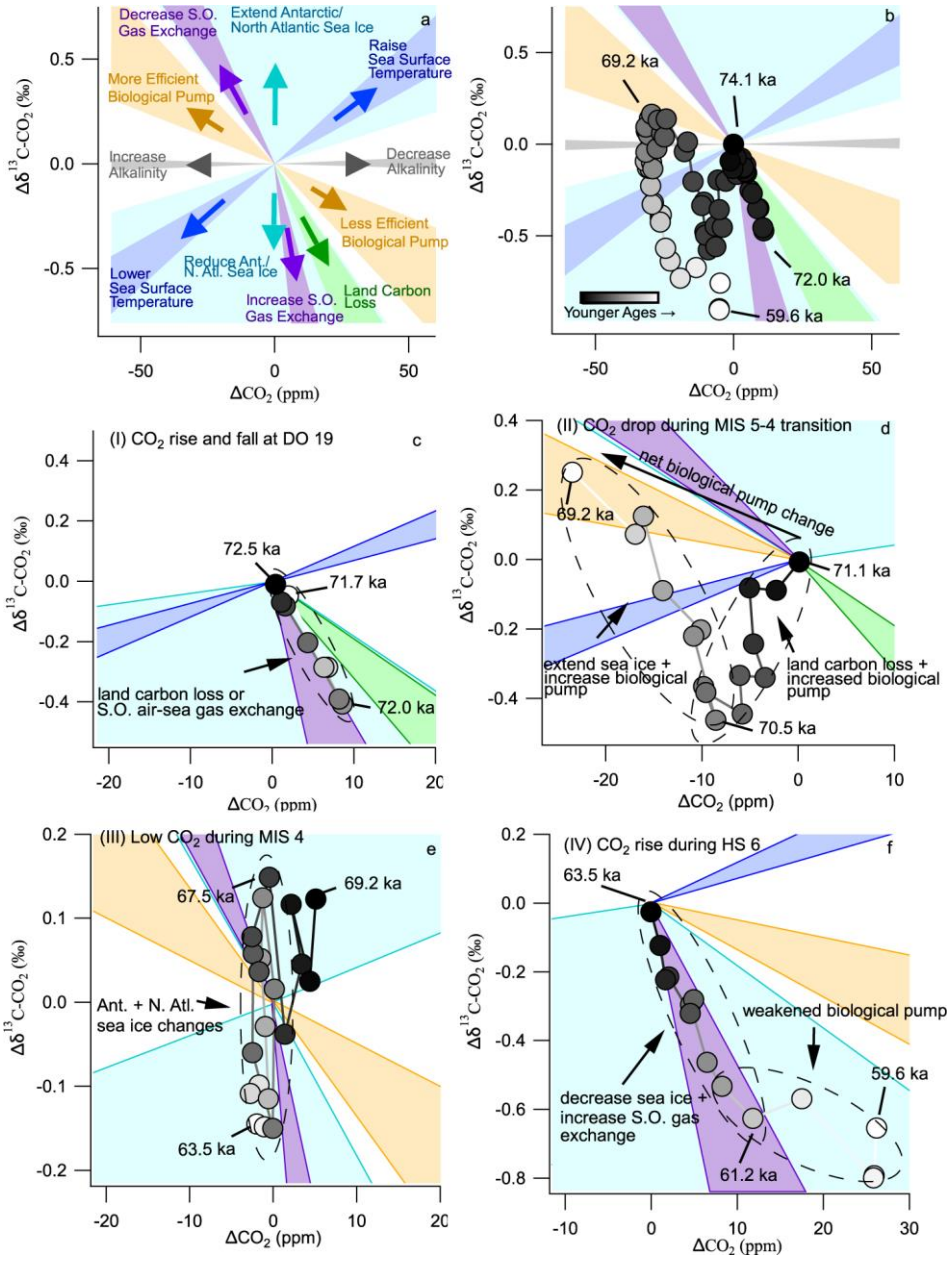

Figure 2. Model framework for interpreting CO_2 and $\delta^{13}C$-CO_2 data. a Compilation of model results estimating the change in $\delta^{13}C$-CO_2 per unit change in CO_2 concentration due to different processes, indicated by shaded regions (see Supplementary information for details). The shading for the processes relevant to our interpretations in each interval is drawn on the following panels. b The temporal evolution of $\delta^{13}C$-CO_2 and CO2 data is indicated by the color gradient on the markers. c–f $\delta^{13}C$-CO_2 and CO_2 data from each of the four intervals I–IV shown in Fig. 1. Note the axes are scaled differently for each panel. c $\delta^{13}C$-CO_2 and CO_2 change during Dansgaard-Oeschger (DO) 19 (interval I in Fig. 1). The data are most consistent with an increase in Southern Ocean air–sea gas

exchange rates or a release of land carbon. d $\delta^{13}C$-CO_2 and CO_2 data for the negative isotope excursion and enrichment during the Marine Isotope Stage (MIS) 5-4 transition (interval II in Fig. 1). The negative excursion is consistent with a large pulse of land carbon combined with increasing efficiency of the biological pump. The growth of Antarctic sea ice and continued deep carbon storage could explain the following enrichment trend. e Oscillations in $\delta^{13}C$-CO_2 during MIS 4 were accompanied by very little change in CO_2 concentration (interval III in Fig. 1), perhaps due to fluctuations in Antarctic sea ice. f The $\delta^{13}C$-CO_2 and CO_2 change during Heinrich Stadial (HS) 6 (interval IV in Fig. 1). The large decrease in δ13C-CO2 is consistent with decreasing Antarctic sea ice and increased air–sea gas exchange in the Southern Ocean. The youngest data (60.9–59.6 ka) are consistent with decreasing efficiency of the biological pump.

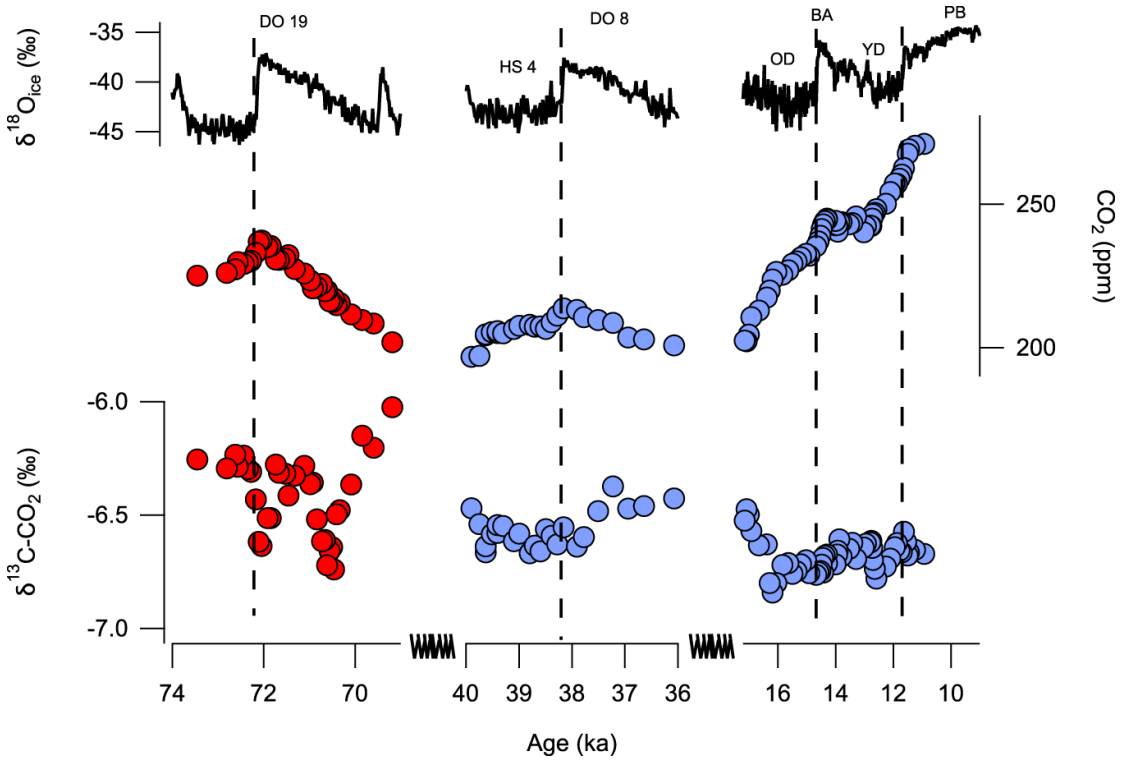

Figure 3. Comparison of abrupt CO_2 changes. The negative isotopic excursion associated with the CO_2 increase at Dansgaard–Oeschger (DO)-19 (red circles, this study) did not occur at other Northern Hemisphere warming events with similar fast CO_2 increases, e.g. DO-8 or the Oldest Dryas (OD)–Bølling–Allerød (BA) transition (blue circles). Water stable isotope data are from North Greenland Ice Core Project (NGRIP).

14. 间冰期结束时，日照引发了大西洋环流的突然减弱

翻译人：夏文月 12231072@mail.sustech.edu.cn

Yin Q Z, Wu Z P, Berger A, et al. ***Insolation triggered abrupt weakening of Atlantic circulation at the end of interglacials****[J]. Science, 2021, 373(6558): 1035-1040.*

https://doi.org/10.1126/science.abg1737

摘要：在许多古气候记录里观测到了间冰期末期的突然的降温，但是引起这种机制的原因仍旧不清楚。使用模型模拟，我们证明了在过去 80 万年间冰期末期时，存在一个由天文因素引发的阈值，低于阈值时，日照量会发生突然变化。当减少的日照量到达临界值，它引发了大西洋径向翻转环流一个强烈的，突然的减弱和平均气温较低的状态，并伴随着持续几千年的高振幅的变化。这个机制涉及到北欧和拉布拉多的的海冰反馈。普遍存在的阈值表明它在终止间冰期末期温暖气候环境起着根本作用。

ABSTRACT: Abrupt cooling is observed at the end of interglacials in many paleoclimate records, but the mechanism responsible remains unclear. Using model simulations, we demonstrate that there exists a threshold in the level of astronomically induced insolation below which abrupt changes at the end of interglacials of the past 800,000 years occur. When decreasing insolation reaches the critical value, it triggers a strong, abrupt weakening of the Atlantic meridional overturning circulation and a cooler mean climate state accompanied by high-amplitude variations lasting for several thousand years. The mechanism involves sea ice feedbacks in the Nordic and Labrador Seas. The ubiquity of this threshold suggests its fundamental role in terminating the warm climate conditions at the end of interglacials.

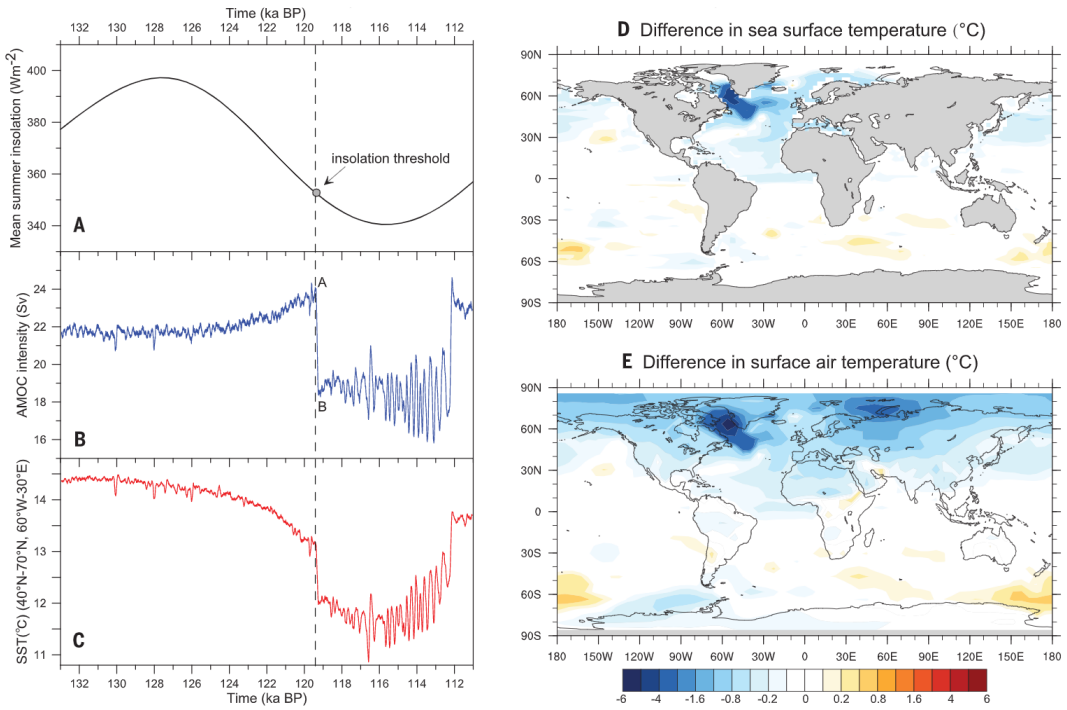

Figure 1. Insolation-only induced variations in AMOC and temperature during MIS-5e. (A) Mean summer insolation averaged over the four latitudes 55°N, 65°N, 75°N, and 85°N; the mean insolation of the half-year NH astronomical summer is obtained by dividing the total irradiation received during the half-year summer by the length of the half-year summer. (B and C) AMOC intensity (B) and annual mean SST (C) in the North Atlantic region. (D) Difference in annual mean SST between points "B" and "A." (E) Difference in annual surface air temperature between points "B" and "A." The results are from the simulation with only insolation varying and CO_2 fixed at 280 ppmv. A 100-year running mean is applied on the simulated AMOC and SST.

15. 末次盛冰期冰盖扩张控制的印度-太平洋暖池干旱加剧

翻译人：刘宇星 11811211@mail.sustech.edu.cn

Xiong Z, Zhai B, Algeo T J, et al. ***Intensified aridity over the Indo-Pacific Warm Pool controlled by ice-sheet expansion during the Last Glacial Maximum****[J]. Global and Planetary Change, 2022: 103952.*

https://doi.org/10.1016/j.gloplacha.2022.103952

摘要：末次盛冰期(LGM)期间印度-太平洋暖池(IPWP)降水变化的强度、方向和原因仍然难以捉摸，尤其是热带或温带因素是否控制了这种降水变化尚无定论。确定 LGM 期间 IPWP 降水的时空分布是解决这一问题的有效策略，但现有降水记录主要来自近海大陆架和边缘海，来自远洋的数据很少。为了填补这一空白，我们分析了菲律宾东部海(EPS)中由叠层硅藻层(LDM)组成的沉积岩芯(WPD-03)中单个 *Ethmodiscus rex* 硅藻壳($\delta^{18}O_{E.\ rex}$)的氧同位素组成。 $\delta^{18}O_{E.\ rex}$ 主要受海面盐度变化控制，因此可以反映整个 IPWP 的公海降水变化。我们的降水替代记录与现有已发布数据相结合，揭示了降水变化的空间模式，表明 LGM 期间整个 IPWP 整体干燥。基于古气候记录与模拟结果的比较，我们提出温带因素（冰盖大小）通过 ENSO 的纬向移动和 ITCZ 的经向迁移相结合来控制 LGM 期间 IPWP 的降水变化。LGM 期间的干旱加剧阻止了海平面下淡水屏障层的形成，因此允许足够的养分进入表层水，刺激 *E. rex* 大量繁殖并随后在 IPWP 中形成 LDM。这些发现表明高纬度气候在 LGM 期间热带水文循环中的重要作用。

ABSTRACT: The magnitude, direction and cause of precipitation changes across the Indo-Pacific Warm Pool (IPWP) during the Last Glacial Maximum (LGM) remain elusive. In particular, it is still inconclusive whether tropical or extratropical factors controlled such precipitation changes. Determining the spatio-temporal distribution of precipitation in the IPWP during the LGM is a valid strategy to address this issue, but the existing precipitation records are dominantly from maritime continents and marginal seas, with few data from pelagic oceans. In order to fill this gap, we analyzed the oxygen isotopic compositions of single *Ethmodiscus rex* diatom frustules ($\delta^{18}O_{E.\ rex}$) from a sediment core (WPD-03) consisting of laminated diatom mats (LDMs) in the eastern Philippine Sea (EPS). $\delta^{18}O_{E.\ rex}$ was controlled mainly by sea-surface salinity variation and, thus,

can reflect open-ocean precipitation changes across the IPWP. Our precipitation proxy records, in combination with existing published data, reveal spatial patterns of precipitation change that indicate overall drying across the IPWP during the LGM. Based on a comparison of paleoclimatic records with modeling results, we propose that extra-tropical factors (ice-sheet size) controlled precipitation variability in the IPWP during the LGM through a combination of zonal shifts of ENSO and meridional migration of the ITCZ. Strong aridity during the LGM prevented formation of a subsurface barrier layer and, hence, allowed accessing of sufficient nutrients to surface waters, stimulating blooms of *E. rex* and subsequent formation of LDMs in the IPWP. These findings suggest an important role for high-latitude climate in the tropical hydrological cycle during the LGM.

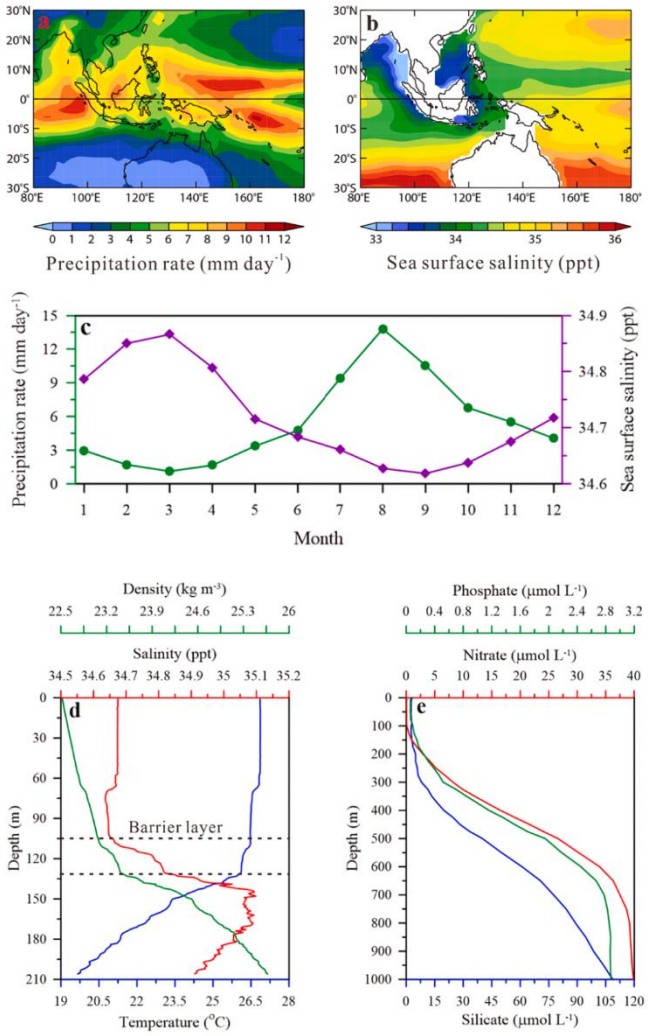

Figure 1. Modern hydroclimate of the IPWP. Annual mean precipitation rate (a) and SSS (b) over the IPWP, and (c) monthly precipitation rate and SSS in the study area (15–21◦N, 136–140◦E). Precipitation and SSS data from historical records (1981–2010) available at www.esrl.noaa.gov/psd/data/gridded/data.cmap.html and www.esrl.noaa.gov/psd/data/gridded/data.godas.html respectively. (d) Depth profiles of

temperature, salinity, and in situ density anomaly in the study site (core WPD- 03); data from this study. (e) Depth profiles of long- term annual mean concentrations of phosphate, nitrate, and silicate around the study site (core WPD- 03); data from the World Ocean Atlas (WOA) 2013 (Garcia et al., 2013).

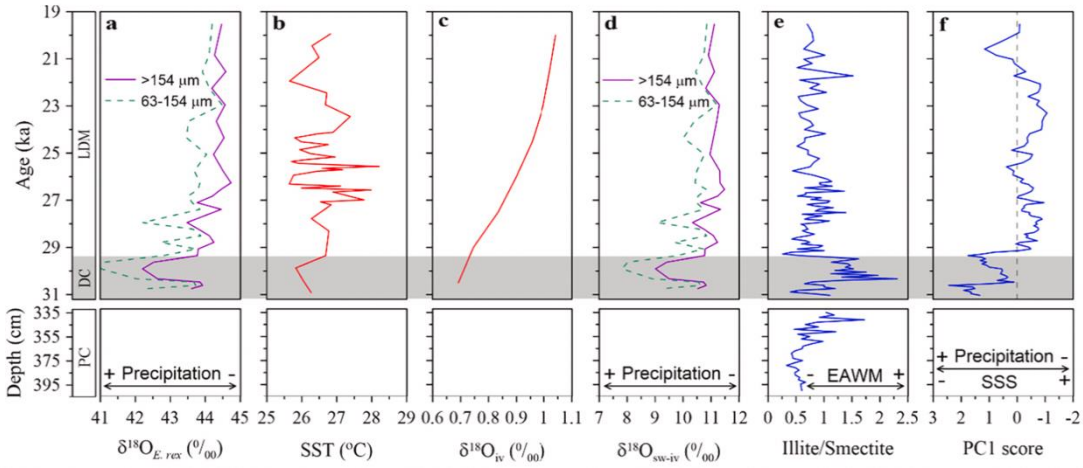

Figure 2. Age-depth profiles for (a) $\delta^{18}O_{E.\ rex}$ in the >154 μm and 63–154 μm fractions, (b) SST from core MD98–2181 (Stott et al., 2002), (c) change in surface-water δ18O related to global ice volume ($\delta^{18}O_{iv}$) (Waelbroeck et al., 2002), (d) $\delta^{18}O_{sw\text{-}iv}$ calculated from $\delta^{18}O_{E.\ rex}$ in the >154 μm and 63–154 μm fractions, (e) illite/ smectite ratio, and (f) PC1 score based on principal component analysis of small diatoms (i.e., excluding mat-forming diatom *E. rex*) (Zhai et al., 2014) in core WPD-03. In (d), $\delta^{18}O_{sw\text{-}iv}$ changes were calculated from $\delta^{18}O_{E.\ rex}$ by accounting for changes in SST (Stott et al., 2002) with a diatom $\delta^{18}O$-temperature coefficient of −0.2‰/◦C (Moschen et al., 2005) and correcting for variations in global ice volume (Waelbroeck et al., 2002). In (f), PC1 score is a measure of SSS in the EPS, with larger values linked to lower SSS (Zhai et al., 2014); the dashed line indicates a PC1 score of zero. LDM: laminated E. rex diatom mats, DC: diatomaceous clay, and PC: pelagic clay.

16. 汉江流域新发现两处早更新世旧石器时代遗址的地层学和年代学

翻译人：聂美娟 12232216@mail.sustech.edu.cn

D. Liu, X. Sun J, C. Lu et al. ***Stratigraphy and chronology of two newly discovered Early Pleistocene Palaeolithic sites in the Hanjiang River Valley, Central China****. Palaeogeography, Palaeoclimatology, Palaeoecology 605 (2022) 111229*

https://doi.org/10.1016/j.palaeo.2022.111229

摘要：在中国中部的秦岭山脉发现了许多露天旧石器时代和人类化石遗址。然而，有一小部分已经被证实可以追溯到早更新世。本研究介绍了秦岭南部汉江流域新发现的丹江口盆地关门岩古石器遗址和云县盆地月亮湖旧石器遗址的地层学和年代学研究。官门岩和月亮湖出土的文物与该地区其他地区发现的旧石器时代早期组合一致。根据磁地层学和黄土-古土壤序列对比，我们的测年结果表明，这两个露天遗址都可以追溯到早更新世。关门岩年代约距今0.787~0.819 Ma（L8），月亮湖上、下旧石器时代文化层年代分别为距今 0.819~0.865 Ma（S8）和距今 0.943~989 Ma（S9）。因此，关门岩和月亮湖有助于填补汉江流域旧石器时代记录的年代空白，使该地区成为记录中国古人类进化重要时期的主要区域。

ABSTRACT: Numerous open air Palaeolithic and hominin fossil sites have been discovered in the Qinling Mountain Range (QMR) in central China. However, a small number have been confirmed as dating to the Early Pleistocene. The present study introduces stratigraphic and chronological studies of the newly discovered Guanmenyan Palae-olithic site, Danjiangkou Basin, and Yuelianghu Palaeolithic site, Yunxian Basin along the Hanjiang River Valley, in the southern QMR. The artefacts recovered from Guanmenyan and Yuelianghu are consistent with Early Palaeolithic assemblages found at other localities in the region. Based on magnetostratigraphy and correlation with the loess-palaeosol sequence from the central Chinese Loess Plateau, our dating results show both open-air sites can be dated to the Early Pleistocene. Guanmenyan is dated ~0.787–0.819 Ma (L8), while the upper and lower Palaeolithic cultural layers of Yuelianghu are dated ~0.819–0.865 Ma (S8) and ~ 0.943–989 Ma (S9), respectively. Thus Guanmenyan and Yuelianghu help to fill a chronological gap in the Palaeolithic record of Hanjiang River Valley and establish the QMR as a major region

documenting this important period of hominin evolution in China.

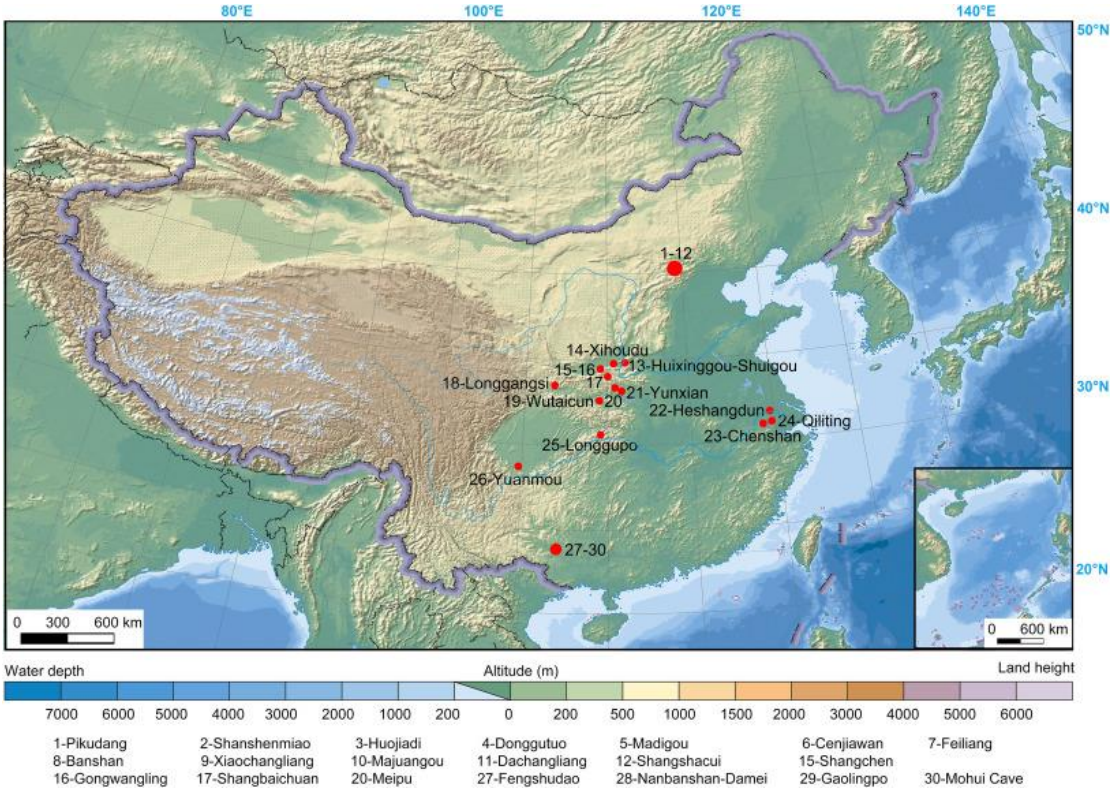

Figure 1. Location of Early Pleistocene archaeological sites in China.

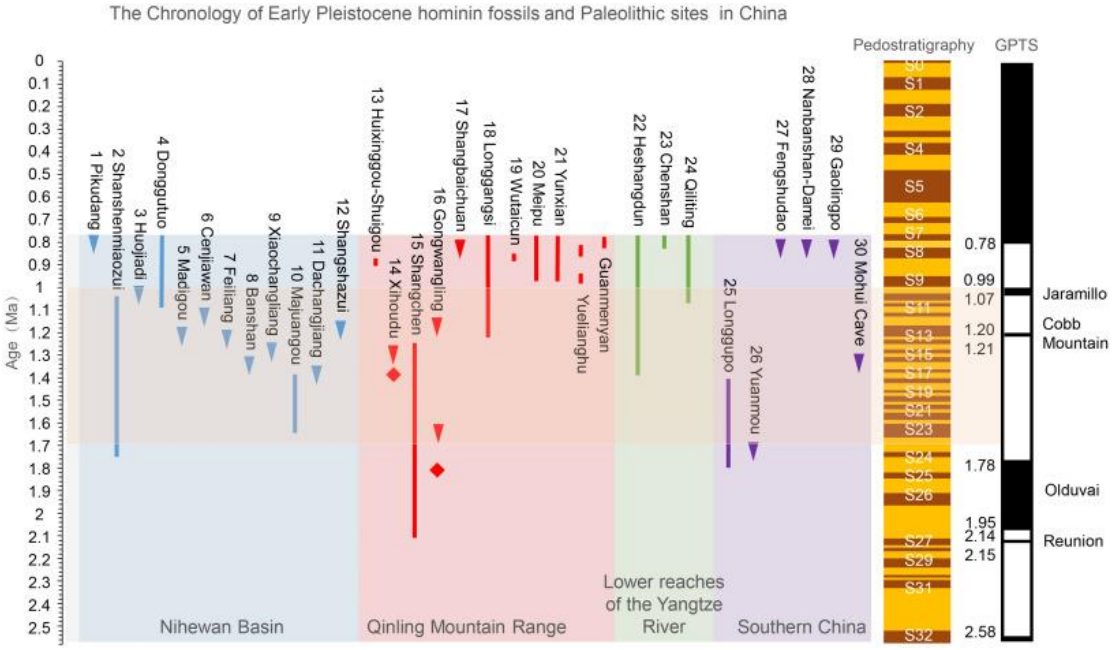

Figure 2. Distribution of the chronology of Early Pleistocene hominin fossils and Palaeolithic sites in China. (the sites marked with blue, red, green, and purple are those in the Nihewan Basin in Northern China, the Qinling Mountain Range (QMR) in Central China, the lower reaches of the Yangtze River in Central China, and Southern China, respectively).